

Metastable spiking networks in the replica-mean-field limit

Luyan Yu

Department of Physics, University of Texas at Austin, Austin, Texas 78712, USA

Thibaud Taillefumier*

*Department of Mathematics and Department of Neuroscience,
University of Texas at Austin, Austin, Texas 78712, USA*

(Dated: May 5, 2021)

Characterizing metastable neural dynamics in finite-size spiking networks remains a daunting challenge. We have recently proposed to address this challenge in the simplifying replica-mean-field (RMF) limit. In this limit, networks are made of infinitely many replicas of the finite network of interest, but with randomized interactions across replica. Such randomization renders certain excitatory networks fully tractable at the cost of neglecting activity correlations, but with explicit dependence on the finite size of the neural constituents. Unfortunately, realistic metastable dynamics typically unfold in networks with mixed inhibition and excitation. To address this point, we extend the RMF computational framework to neural networks modeled by point processes with exponential stochastic intensities. Within this framework, we show that metastable finite-size networks admit multistable RMF limits, which are fully characterized by stationary firing rates. Technically, these stationary rates are determined as solutions to a set of delayed differential equations under certain regularity conditions that any physical solutions shall satisfy. We solve this original singular-perturbation problem by adapting the resolvent formalism to our delayed setting. Importantly, we find that these rates specify probabilistic pseudo-equilibria which accurately capture the neural variability observed in the original finite-size network. We also perform the analysis of the stochastic bifurcation of a bistable neural network in terms of static phase transition of its RMF limits. In turn, we expect to leverage the static picture of RMF limit to infer purely dynamical features of metastable, finite-size networks, such as transition rates.

I. INTRODUCTION

One of the striking features of neural activity is its high degree of trial-to-trial variability in response to identical stimuli [1, 2]. In principle, there are two nonexclusive explanations for such variability: neural variability can arise from inherently noisy transduction mechanisms, such as photon counting noise or faulty synaptic transmissions [3, 4]; or neural variability can reflect fluctuations of unmonitored variables, such as global attention state or cross-sensory influences [5, 6]. Thus, neural variability can be seen as a nuisance to faithful information processing or as an integral part of neural computations [7–9]. In particular, neural variability is a key determinant of the metastable dynamics thought to support computations in neural networks [10, 11]. However, understanding the possible roles of variability in a computation remains a conundrum. This is partly due to the lack of mechanistic models for which variability can be quantified in relation to a few biophysically relevant neural features.

Modeling neural variability involves considering the activity of neurons as stochastic processes [12, 13]. Accounting for the spiking nature of neural interactions motivates adopting the framework of stochastic point processes. The simplest instances of such models are Poisson processes for which spike generation is governed by

a deterministic firing rate function. This function is effectively computed as an average over spiking deliveries. More realistic models with a role for individual spiking events, require considering the instantaneous firing rate as a stochastic variable, formally defined as the stochastic intensity of a point process [14, 15]. Specifying a mechanistic model for a neural network then consists in relating neuronal stochastic intensities to the past states of the network. Such stochastic-intensity-based models have been successful in accounting for many key problems in neural coding such as measuring the regularity of neuron spiking events [16], decoding velocity and direction from the motor cortical recordings [17] and predicting stability of the neuronal dynamics [18].

Quantifying variability in stochastic neural network models often relies on drastic simplifying approximations, typically obtained in the thermodynamic-mean-field (TMF) limit [19–22]. This limit considers infinite-size networks whereby individual neurons receive a diverging number of vanishingly small synaptic inputs, with synaptic strengths typically scaling in inverse proportion of the number of inputs. Unfortunately, TMF limits fail to capture the variability of finite-size neural networks when stochasticity is shaped by the discrete nature of the interacting neuronal components. This limitation is especially concerning in lights of recent findings suggesting that neurons are primarily driven by a limited number of strong inputs during meaningful computations [23, 24].

In a recent work [25], we introduced the replica-mean-field (RMF) framework by adopting the *multiply-and-*

* Corresponding author; ttaillef@austin.utexas.edu

conquer approach. Distinct from the ideas extensively used in statistical physics [26, 27], our inspiration for replication originated from the study of communication systems [28, 29]. In the RMF framework, we consider limit networks made of infinitely many replicas with the same basic finite network structure, but with randomized routing of the interactions across replicas. In this process, neurons become asymptotically independent subjected to Poissonian bombardment [30]. Thus, the RMF framework preserves the stochastic nature of inputs, which allows to capture some of the finite-size effects shaping neural variability. By contrast, TMF limits erase all inputs stochasticity when averaged over infinite networks.

Our introductory work [25] demonstrated how RMF limits can capture finite-size effects in the stationary dynamics of certain neural networks. However, this was only done for a restricted class of excitatory models with limited range of dynamics. Here, we develop the RMF computational framework for a new class of models with mixed inhibition and excitation and we demonstrate that the RMF approach applies to an extended range of dynamics, including metastable ones. In our model, referred to as the exponential Galves-Lochérbach (EGL) models, neurons integrate finite-size spiking interactions via a continuously relaxing internal variable, mimicking the membrane potential. Moreover, the instantaneous neuronal firing rate is determined as an exponential function of the neuron's internal variable. Finally, the internal variable resets to base level upon spiking, thereby implementing a refractory. Thus-defined, EGL models belong to a larger class of generalized linear models studied in computational neuroscience [18].

The simplifying assumptions of the RMF framework enable us to calculate the stationary mean firing rates as a function of the network parameters. In the RMF setting, these rates fully parametrize the neural dynamics as sufficient statistics for the stationary distribution of the network states. Thus, we are able to characterize the neural variability by computing the moments of the stochastic intensities and of the internal variables from the knowledge of the stationary rates. These calculations can be performed in the RMF limits for any network topologies. We find that the RMF estimates agree well with the exact, event-driven simulations of the original finite-size network [31, 32]. Surprisingly, our formulation, based upon the assumption of stationarity, can also capture the dynamics of metastable networks. Metastable networks exhibit dynamics characterized by fluctuations around pseudo-equilibrium states at small time scales and sharp transitions between pseudo-equilibria at larger time scales. In the RMF limit, metastability turns into multistability as the self-consistent equations admit multiple solutions for stationary firing rates. The emergence of multistability corresponds to the divergence of transition rates between pseudo-equilibria in the RMF limit. Thus, just as in TMF limits, dynamical ergodicity breaks down in infinite-size metastable networks, which display distinct stationary distributions. However, by contrast

with TMF limits, RMF limits preserve the stochastic nature of inputs, so that these distinct stationary distributions can serve to approximate the neural variability of the original metastable dynamics. We demonstrate this point for a bistable neural network whose structure is motivated by the study of perceptual rivalry in neuroscience [33]. Remarkably, the RMF limit can predict the variability of such networks even when the metastability originates from as few as 40 strongly interacting neurons. These results are obtained when subjecting the 40 neurons to weak TMF-like excitatory inputs, modeling modulation by uncorrelated background inputs [23, 24]. We also show that our RMF approach can numerically detect the phase transition from monostability to bistability.

Methodology-wise, we derive the self-consistent equations for the RMF stationary rates of EGL networks in the form of delay differential equations (DDEs). Unlike in standard settings, these DDEs do not come equipped with a notion of initial conditions on a delayed range to specify their solutions [34–37]. Rather, we determine these solutions solely by imposing the regularity and normalization conditions that any probabilistic model should satisfy. To our knowledge, there are no closed form solutions to this problem and no standard method for numerically solving it. We develop such a method by adapting the resolvent formalism [38–40] to write the RMF stationary firing rates as divergent series. In turn, we compute the resulting rates via an iterative scheme utilizing Padé approximants summation.

This work is structured as follows. In Sec. II, we introduce the notion of stochastic intensity, formulate RMF framework, and establish the RMF self-consistent equations. In Sec. III, we discuss these equations from a numerical point of view and propose to use Padé approximants summation for numerical estimation. In Sec. IV, we demonstrate our computational approach with a focus on finite-size effect in metastable dynamics and compare them with the TMF approximations. Finally, in Sec. V, we discuss the biophysical relevance of our modeling approach and introduce some future computational extensions.

II. MODELING AND THEORY

A. Stationary stochastic network dynamics

In this work, we model the stochastic spiking activity of a neuron i as a point process $N_i(t)$, which registers spiking occurrences as time-indexed Dirac-delta functions. In other words, $N_i(t) = \sum_k \delta(t - t_{i,k})$, where $t_{i,k}$ denotes a sequence of spiking times of neuron i . The probability to find a spike in the infinitesimal time interval $[t, t + dt]$ can be written as $\lambda_i(t)dt$, where $\lambda_i(t)$ is informally defined as the instantaneous firing rate of neuron i . This rate $\lambda_i(t)$ depends on the past history of the network, e.g., on the last time neuron i spiked and on the inputs it may have received since that time. As

such, $\lambda_i(t)$ is actually a nonnegative random variable and $t \mapsto \lambda_i(t)$ is formally defined as the stochastic intensity process governing the point process $N_i(t)$ [14, 15].

Our goal is to characterize the typical distribution—or at least approximate the first moment—of $\lambda(t)$ for certain intensity-based model of neuronal networks, referred to as exponential Galves-Löcherbach (EGL) networks. General Galves-Löcherbach models can be seen as interacting Hawkes processes complemented with individual post-spiking reset rules [41, 42]. Among these models, EGL networks are those for which the stochastic rate $\lambda_i(t)$ is exponentially related to a neuron-specific internal variable $x_i(t)$, which integrates past neuronal interactions. Specifically, we have

$$\lambda_i(t) = h_i e^{a_i x_i(t)}, \quad (1)$$

where h_i and a_i are positive constants. The dynamics of the internal variable $x_i(t)$ is as follows: Whenever neuron i spikes, $x_i(t)$ instantaneously resets to zero, erasing all memory effects at the individual neuron level. At the same time, neurons $j \neq i$ register the instantaneous deliveries of Dirac delta impulses in their internal variables $x_j(t)$ via synaptic strengths μ_{ji} . This registration proceeds in a leaky fashion so that $x_i(t)$ obeys the linear stochastic differential equation

$$\begin{aligned} x_i(t) &= x_i(0) - \frac{1}{\tau_i} \int_0^t x_i(s) \, ds \\ &+ \sum_{j \neq i} \mu_{ij} N_j(t) - \int_0^t x_i(s^-) N_i(ds), \end{aligned} \quad (2)$$

where τ_i denotes the relaxation time of the neuronal internal variable to zero. Observe that the last integral term in Eq. (2) implements the post-spiking reset rule to zero. Moreover, note that in view of Eq. (2), h_i appears as the (nonzero) base spiking rate of neuron i , whereas a_i models its excitability.

To sum up, we model a neuronal network as a directed weighted graph whose nodes are neurons and whose directed edges are synaptic weights μ_{ij} from neuron j to i . Within the network, the state of a neuron i is given by its internal variable x_i , which determines the neuronal instantaneous firing rate λ_i via the exponential relation Eq. (1). The individual neuronal dynamics consists of three components: (i) interaction, (ii) reset, and (iii) relaxation. (i) When neuron i fires, x_j , $j \neq i$, updates

to $x_j + \mu_{ji}$. (ii) At the same time, x_i resets to zero. (iii) In between spikes, each $x_i(t)$ relaxes towards zero whose time constant is τ_i . Thus specified, the dynamics of EGL networks defines a continuous-time Markov chain. Considerations from the regenerative theory of Markov chains shows that in the presence of relaxation, i.e., whenever $\max_i \tau_i < \infty$, this chain is ergodic [25, 43]. This means that there is a unique stationary distribution characterizing typical network states.

B. Replica mean-field limits

A key benefit to considering EGL models is that they naturally accommodate inhibition by allowing for negative synaptic weight $\mu_{ij} < 0$. This is by contrast with linear LGL models for which including inhibition conflicts with the required nonnegativity of the rate functions $\lambda_i(t)$. Unfortunately, just as for their linear counterparts, an exact analytical treatment of the finite-size EGL models hinders on the complex structure of activity correlation. This limitation motivates considering EGL networks in some simplifying limit of the thermodynamic mean-field type. In this work, we consider EGL networks in the replica-mean-field (RMF) limit. This limit procedure, introduced in [25], is distinct from the classical replica approach in statistical physics [26, 27] and inspired from network theory [28, 29]. Just as standard thermodynamic mean-field limits [19–22], RMF limits erase correlations among neurons, allowing for an analytical treatment. However, unlike standard thermodynamic mean-field (TMF) limits, RMF limits preserves some feature of the finite size of the network, such as finite-size synaptic weights [25]. The latter point is the core reason to consider RMF limits.

The RMF limit of a EGL network comprises an infinite number of replicas of the original systems (Fig. 1) [44]. By original system, we mean the K -neuron network with EGL dynamics described by Eq. (2). The R -replica model is obtained by considering that a neuron i within each replica r , $1 \leq r \leq R$, follows the same autonomous dynamics of as neuron i in the original system. However, the key difference with the original system is that upon spiking, a neuron i from replica r interacts with neurons (j, q) , $j \neq i$, via the original weights μ_{ji} but in replicas q , chosen uniformly at random. Formally, this corresponds to the following set of stochastic equations

$$x_{i,r}(t) = x_{i,r}(0) - \frac{1}{\tau_i} \int_0^t x_{i,r}(s) \, ds + \sum_q \sum_{j \neq i} \mu_{ij} \int_0^t \mathbb{1}_{\{v_{r,ij}(s)=r\}} N_{j,q}(ds) - \int_0^t x_{i,r}(s^-) N_{i,r}(ds), \quad (3)$$

where for all $s \geq 0$, $0 \leq r, q \leq R$, $1 \leq i \neq j \leq K$, $v_{r,ij}(s)$ are independent random variable uniformly distributed over $\{1, \dots, R\}$. These random variables are routing ad-

dresses specifying that when neuron (j, r) spikes at time s , it targets a neuron of type i in replica $v_{r,ij}(s)$.

Intuitively, the randomization of interactions present

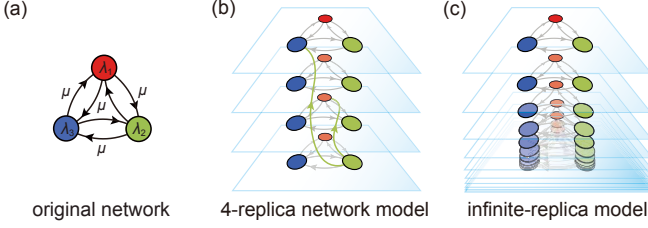


FIG. 1. **Physical RMF models.** Panel (a): Original networks of $K = 3$ neurons. Panel (b): First-order, finite-replica model with $r = 4$ replicas. When a neuron spikes (green neuron), it interacts with downstream neurons sampled uniformly at random across replicas. Panel (c): RMF models are obtained in the limit of an infinite number of replicas and represent infinite-size physical models supporting RMF dynamics.

in Eq. (3) degrades statistical dependences between neurons and across replicas. For large number of replicas, i.e., in the RMF limit, the neurons become asymptotically independent. Moreover, each neuron of type i asymptotically receives inputs from neurons of type $j \neq i$ with Poissonian statistics across replica. For often being only conjectured, the emergence of this simplified limit dynamics is referred to as the “Poisson Hypothesis” in network theory [45]. The Poisson Hypothesis was recently established rigorously for generic RMF limits, including EGL models [30]. Under the Poisson Hypothesis, in RMF limits of EGL networks, a neuron i from a representative replica admits an effective dynamics given by

$$x_i(t) = x_i(0) - \frac{1}{\tau_i} \int_0^t x_i(s) \, ds \quad (4)$$

$$+ \sum_{j \neq i} \mu_{ij} P_j(t) - \int_0^t x_i(s^-) N_i(ds),$$

where the point processes $P_j(t)$ are independent Poisson processes with stationary firing rate β_j . Thus, at fixed network structure, the dynamics $x_i(t)$ only depends on the network background activity via the rates $\{\beta_j\}_{j \neq i}$. To be consistent under assumption of stationarity, these rates must collectively satisfy the system of equations

$$\beta_i = h_i \mathbb{E}[e^{a_i x_i}] = \mathcal{F}_i(\{\beta_j\}_{j \neq i}), \quad 1 \leq i \leq K, \quad (5)$$

where the notation \mathcal{F}_i emphasizes that β_i is evaluated as a function of the rates $\{\beta_j\}_{j \neq i}$. In the following, we will refer to \mathcal{F}_i as rate-transfer functions. The fact that rate quantities characterize alone the dynamics is a feature of RMF limits. Specifying RMF limits for EGL networks consists in solving the self-consistent system Eq. (5). This is the purpose of this work.

C. Delay differential equations

Heretofore, we have only considered RMF limits and their associated self-consistent system Eq. (5) formally.

To exploit RMF limits computationally, one must find explicit forms for the rate-transfer functions featured in Eq. (5). Determining these explicit forms is the main challenge of the RMF approach and is the topic of the next section. Here, as a first step toward this goal, we establish functional relations between the stationary rates β_i via probabilistic arguments. Specifically, we exploit the rate-conservation principle for point processes [46, 47] to exhibit a system of delay differential equations (DDEs) featuring the rates β_i .

In a nutshell, the rate-conservation principle states that in the stationary regime, any real-valued function of the network states reaches an equilibrium where there is a balance between its rate of increase and its rate of decrease. By virtue of the Poisson Hypothesis for RMF limits, we can apply the rate-conservation principle to any function of the internal states $x_i(t)$ independently. A natural choice is to consider exponential function $x_i(t) \mapsto e^{ux_i(t)}$, whose stationary expectation defines the moment-generating function (MGF) $L_i(u) = \mathbb{E}[e^{ux_i}]$. The MGF L_i fully specifies the stationary distribution of $x_i(t)$ and is a well-behaved analytical function when it exists on an open interval containing zero. In the following, we assume that the MGF L_i always exists in the RMF limit. By this, we mean that the MGF L_i remains finite on an open interval containing zero, which implies analyticity in zero so that $x_i(t)$ admits moments of all order.

As a process, $t \mapsto e^{ux_i(t)}$ satisfies a stochastic equation which can be deduced from Eq. (2) as

$$e^{ux_i(t)} - e^{ux_i(0)} = - \frac{u}{\tau_i} \int_0^t x_i(s) e^{ux_i(s)} \, ds$$

$$+ \sum_{j \neq i} (e^{u\mu_{ji}} - 1) \int_0^t e^{ux_i(s^-)} P_j(ds)$$

$$+ \int_0^t (1 - e^{ux_i(s^-)}) N_i(ds). \quad (6)$$

The three consecutive integral terms in the RHS correspond to continuous relaxation, independent Poisson bombardments, and post-spiking reset, respectively. At stationarity, we have $\mathbb{E}[e^{ux_i(t)}] = \mathbb{E}[e^{ux_i(0)}]$, so that the rate-conservation principle implies that the RHS has zero stationary expectation. In turn, we can interpret the stationary expectation of the three integral terms in term of the MGF L_i (see Appendix A for derivation). Ultimately, the rate-conservation principle takes the form of the following linear DDE

$$\frac{u}{\tau_i} L'_i(u) - V_i(u) L_i(u) - (\beta_i - h_i L_i(u + a_i)) = 0, \quad (7)$$

where we have introduced $V_i(u) = \sum_{j \neq i} \beta_j (e^{\mu_{ji} u} - 1)$ for brevity. The above equation is similar to the ODEs appearing for LGL models with the major difference of being nonlocal via the term $L_i(u + a_i)$. This nonlocality is due to the exponential form of Eq. (1) for the rate $\lambda_i(t)$ as interpreting the expected reset term in Eq. (6)

involves evaluating

$$\mathbb{E} \left[\lambda_i(s) e^{ux_i(s)} \right] = \mathbb{E} \left[e^{a_i x_i(s)} e^{ux_i(s)} \right] = L_i(u + a_i). \quad (8)$$

In the framework of perturbation theory, Eq. (7) can be viewed as a singularly perturbed delay differential equation, whose perturbation parameter h_i , unlike many other more common cases, is on the delay term. To see this, note that $\beta_i = h_i \mathbb{E}[e^{a_i x_i}] = h_i L_i(a_i)$, so that Eq. (7) reads

$$\frac{L'_i(u)}{\tau_i} - \frac{V_i(u)}{u} L_i(u) + h_i \left(\frac{L_i(u + a_i) - L_i(a_i)}{u} \right) = 0, \quad (9)$$

where h_i appears as the coefficient of a forward discrete derivative. In the limit of $h_i \rightarrow 0$, Eq. (9) becomes an analytically solvable, first-order homogeneous ODE. Observe that Eq. (7) incidentally exhibits the additional role of $1/\tau_i$ as a singular perturbation parameter. In the limit of $\tau_i \rightarrow \infty$, Eq. (9) becomes a pure delay equation, which resists closed-form resolution. For this reason, h_i will play the central part as a perturbation parameter.

The main caveat to solving Eq. (9) for generic EGL models ($1/\tau_i, h_i \neq 0$) is that the nonlocality of the DDEs Eq. (7) precludes a direct analytical treatment, while posing problems with respect to solution uniqueness. To see this, observe that if one interpret the variable u as a time parameter, the nonlocal term $L_i(u + a_i)$ formally introduces a negative delay $-a_i$. Due to the negativity of this delay, one can only solve the DDE Eq. (9) of the form $x'(u) = f(x(u), x(u + a_i))$ backward, i.e., for decreasing value of u . Moreover, such solutions are only unique given the knowledge of initial conditions on an interval of duration a_i . However, in our probabilistic setting, we will see that there is a natural representation for a probabilistically interpretable solution to Eq. (9), with no need to specify any initial conditions on an interval.

D. Self-consistent equations via resolvent formalism

Our goal is to characterize the unique MGF solution to the DDE Eq. (7). Achieving this goal will allow us to give an explicit form to the rate-transfer functions formally defined by Eq. (5). For simplicity, we omit all the neuronal indices whenever possible in the following. For instance, we will denote the output stationary firing rate of neuron i by β when unambiguous. Our strategy is to adapt the resolvent formalism to our delayed framework [48] in three steps.

First, we consider the forward discrete derivative term $(L(u + a) - L(a))/u$ as a known inhomogeneous term so that we can view Eq. (9) as a linear ODE about L . Then, the method of the variation of parameters yields integral forms for L involving its shifted version $L(\cdot + a)$, but also some undetermined initial condition. We resolve the latter indeterminacy by selecting the only solution taking value $L(a) = \beta/h$. This yields the following integral

equation

$$L(u) = \frac{\beta q(u)}{h} - h\tau \int_a^u \frac{q(v)}{q(v)} \frac{L(v + a) - L(a)}{v} dv, \quad (10)$$

where q denotes the homogeneous solution to Eq. (7) excluding the forward discrete derivative term: $q(u) = \exp(\tau \int_a^u V(v)/v dv)$.

Second, in view of Eq. (10), we define the auxiliary function $H(u) = (L(u + a) - L(a))/u$. Substituting $H(u)$ into Eq. (10), we obtain the following integral equation for H

$$H(u) = \frac{\beta}{h} \left(\frac{q(u + a) - 1}{u} \right) - q(u + a) \left[\frac{h\tau}{u} \int_a^{u+a} \frac{H(v)}{q(v)} dv \right], \quad (11)$$

where the delayed nature of the problem appears via the nonlocal upper integration bound. Moreover, observe that the inhomogeneous term in Eq. (11) is analytic, whereas the integral term is analytic whenever H is analytic. Eq. (11) is the basis for adapting the resolvent formalism to our delayed framework. Indeed, defining the sequence of iterated kernels

$$Q_m(u) = q(u + a) \left[\frac{1}{u} \int_a^{u+a} \frac{Q_{m-1}(v)}{q(v)} dv \right], \quad (12)$$

with $Q_0(u) = (q(u + a) - 1)/u$, we can formally write the solutions to Eq. (11) as the series

$$H(u) = \frac{\beta}{h} \sum_{m=0}^{\infty} (-h\tau)^m Q_m(u), \quad (13)$$

where h appears as a perturbation parameter via the dimensionless quantity $h\tau$ (see Sec. IV A 1 below). Note that the kernels Q_m are independent of h but also of β , the yet-to-be determined output firing rate. Note also that as the Q_m are analytic in u , H is an analytic function around zero as soon as the series converges uniformly on an open disk containing zero. We conjecture that this is always the case.

Third, we specify β as a function of the input parameters by exploiting the normalization constraint of the MGF: $L(0) = 1$. From the definition of H above, we have that $-aH(-a) = L(0) - L(a) = 1 - \beta/h$. Thus, together with Eq. (13), we must have

$$\frac{h}{\beta} = 1 - a \sum_{m=0}^{\infty} (-h\tau)^m Q_m(-a), \quad (14)$$

where the dependencies on the input rates β_j , $j \neq i$, are mediated by the kernels Q_m . Observe that in the absence of inputs, i.e., for $V(u) = 0$, we have $q(u) = 1$ so that all the terms $Q_m(-a) = 0$ and we recover consistently that $\beta = h$ as the internal state x remains identically zero. Eq. (14) determines the rate-transfer function \mathcal{F} of a neuron in a feedforward network. When considering a recurrent network, these rate-transfer functions define the sought-after self-consistency equations (5), which

must be jointly satisfied. These equations take the explicit forms:

$$\beta_i = h_i \left[1 - a_i \sum_{m=0}^{\infty} (-h_i \tau_i)^m Q_{i,m}(-a_i; \{\beta_j\}_{j \neq i}) \right]^{-1}, \quad (15)$$

where we have indexed all neuron-specific quantities and highlighted the dependencies on the input rates β_j , $j \neq i$. In the following, we will refer to the quantities computed by Eq. (15) as “RMF calculation”. In the next section, we discuss the numerical method used to solve Eq. (15).

III. NUMERICAL METHOD

A. Divergent perturbative series

The formal series expansion Eq. (15) suggests a natural numerical scheme to compute β . At stake is to compute the values $Q_m(-a)$, $m \geq 0$, in order to approximate the output rate β by truncating the series $\sum_{m=0}^{\infty} Q_m(-a) y^m$ at $y = -h\tau$. As the functions Q_m are defined iteratively via the nonlocal integral relation given in Eq. (12), the numerical computation of $Q_m(-a)$ requires mesh grids in different ranges for different m . Specifically, calculating $Q_m(-a)$ requires the knowledge of Q_{m-1} in the range $[0, a]$, which then requires Q_n to be known in the range $[a, (m-n)a]$, $0 \leq n \leq m-2$. Therefore, denoting the ultimate order of the approximation by M , we first evaluate Q_0 , which we know in closed form, on some mesh grid in the range $[0, Ma]$. Then, we proceed to sequentially evaluate Q_{n+1} for increasing order by numerical integration of Q_n via Eq. (14) over the range $[0, (M-n)a]$. After repeating this iteration M times, we collect $Q_0(-a), Q_1(-a), \dots, Q_M(-a)$. We will discuss how to choose the approximation order M in the next section (Sec. III B).

In principle, one can hope to compute β by direct summation of the Taylor series involving the collected coefficients $\{Q_m(-a)\}_{m=0}^M$. The convergence of such series is justified within the resolvent-like formalism if the functional map $Q_m \mapsto Q_{m+1}$ given by (12) is a contraction [49]. Unfortunately, this condition does not hold for moderately large excitation as shown in Fig. 2, which estimates the radius of convergence of the series as $r = \lim_{m \rightarrow \infty} r_m$ with $1/r_m = |Q_m(-a)|^{1/m}$. Fig. 2(a) shows that $1/r_m$ grows superexponentially when the neuron receives excitatory inputs. This indicates a zero radius of convergence so that direct summation using Eq. (14) will fail whenever $h \neq 0$. By contrast, Fig. 2(b) shows that $1/r_m$ admits a finite limit when the neuron is subjected to inhibitory inputs alone. This is also true for weak inputs, as shown in Fig. 2(c, d).

This numerical evidence suggests that β , as a function of the perturbation parameter h , is non-analytic in zero whenever the neuron is driven by strong excitatory inputs. Moreover, even when the series has finite radius,

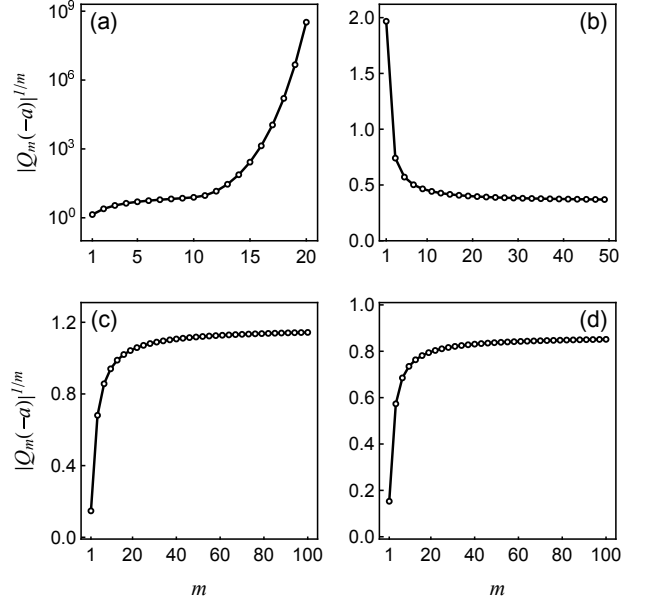


FIG. 2. **Plots of $1/r_m = |Q_m(-a)|^{1/m}$ v.s. m .** This figure is the numerical values of the series coefficients subjected to different types of inputs. The input rates $\beta_{e,i} = 0.5$ kHz are the same across all four panels. In panel (a), the neuron is subjected to an excitatory input with $\mu_e = 3$. The superexponential growth of $1/r_m$ is clearly manifested in this log-scale plot. In panel (b), the neuron is subjected to an inhibitory input with $\mu_i = -3$. In panel (c, d), the neuron is subjected to a weak excitatory and inhibitory input with $\mu_e = 0.3$ and $\mu_i = -0.3$ respectively. In these three cases, $1/r_m$ converges to finite values. Parameters: $h = 1$ Hz, $a = 0.1$, $\tau = 10$ ms.

we will see that the convergence is only possible for a very restricted range of inputs (see Sec. III B). This is due to h being a singular perturbation parameter when $h \rightarrow 0$. There exists different techniques to approximate the general solution of singular perturbation problems such as, e.g., multi-scale analysis [50] or matched asymptotics of distinguished solutions [51]. Here, we are mostly concerned with evaluating the output rates β for a large range of input parameters, rather than giving a full MGF solution. For this reason, we will content ourselves with leveraging the knowledge of the divergent series to form convergent approximations via Padé theory [52, 53].

B. Padé approximants

Direct Taylor series summation fails for neurons whose drive is dominated by excitation. This is a major drawback as network-level nonlinear dynamics typically involves regimes in which subset of neurons are strongly excited. This is particularly the case for multistable systems where active groups of neurons are stabilized by strong recurrent excitation. In that respect, we will verify in Sec. IV B that this setting is sufficient for multistability to emerge in the RMF limit of EGL networks.

This will require evaluating rate-transfer functions via Padé approximants summation.

Divergent series may emerge from an ‘invalid Taylor expansion’, typically because the evaluated point is outside the radius of convergence, or the function is singular in the first place. The regularity of polynomials is a bless but also a curse when dealing with functions with singularities. Instead of using polynomials as in Taylor series, Padé approximants utilize rational functions, which naturally incorporates singularities at the zeros of the denominator polynomials. This trade-off—including the singularity and disregarding the regularity—makes Padé approximants more expressive. To extract the information of the original function from the divergent series, we would use Padé approximants to re-approximate the series in the form of rational functions. To be specific, let the Padé approximant of the n -th partial sum $\sum_{m=0}^n Q_m(-a)y^m$ be $P_n(y)$. Evaluating the approximants at $y = -h\tau$ would lead us to a sequence: $P_0(-h\tau), P_1(-h\tau), P_2(-h\tau), \dots$. If the Padé approximants converge, we assign the limiting value $\lim_{n \rightarrow \infty} P_n(-h\tau)$ to be the functional value of the original divergent series. Numerically, we can choose the cut-off M so that $|P_M(-h\tau) - P_{M-1}(-h\tau)|$ is within error tolerance and let $P_M(-h\tau) \approx \sum_{m=0}^M Q_m(-a)(-h\tau)^m$. For more details, the reader may refer to references [52, 53].

We compare the parametric regimes where the direct Taylor series summation and the Padé approximants summation converge to the correct result, respectively. We consider a single neuron subjected to an excitatory input of varying rate β_e and strength μ_e . For each parametric point (β_e, μ_e) , we test if the computed output rate β lies within one standard deviation of the simulated β . The results are shown in Fig. 3 where each panel corresponds to a different set of h and a . From Fig. 3(a), we observe that the direct method indeed works only when the excitatory inputs are weak. The contour curve of the convergent parametric regime is approximately linear in this log-scale plot, which means the maximal computable excitatory input rate β_e is exponentially decreasing when we increase the excitatory synaptic strength μ_e . The Padé approximant summation, on the other hand, yields a significantly better coverage on the (β_e, μ_e) parametric space. Although the maximal β_e still decreases exponentially when μ_e is large, the decay is much slower, especially in the low and moderately high rate regime. Fig. 3(b) shows the convergent parametric regimes with $a = 0.2$ doubled from $a = 0.1$. Both of the regimes shrink into half, which is expected considering that in Eq. (1), only the product of a and μ is important. In Fig. 3(c), the base spiking rate h changes to 50 Hz from 1 Hz. We notice that in high β_e regime, the convergent regime of direct method is further suppressed. This is understandable since the larger $h\tau$ tends to lie outside the radius of convergence earlier as μ_e increases. The superiority of Padé method is manifested more in this case since in high β_e regime, the convergent regime only shrinks slightly and is not affected as much as that of the direct method.

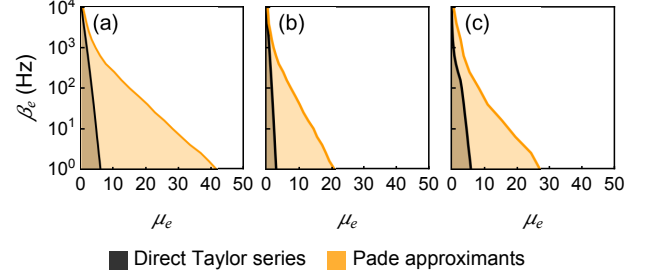


FIG. 3. **Convergent parametric regimes.** The comparison of the convergent parametric regimes for the direct Taylor series summation and Padé approximants summation. The convergence regimes are shaded in different colors and their envelope curves are shown. The vertical axis is in log scale. The convergence of each parametric point (β_e, μ_e) is determined by whether or not the computed β value is within one standard deviation of the simulated β value. In panel (a), $h = 1$ Hz, $a = 0.1$; panel (b) $h = 1$ Hz, $a = 0.2$; panel (c) $h = 50$ Hz, $a = 0.1$. Parameters: $\tau = 10$ ms.

IV. RESULTS

A. Input/output transfer function

1. Nonlinear corrections and reset mechanism

The derivation of Eq. (9) shows that its delayed nature is due to the presence of a post-spiking reset mechanism. This post-spiking reset mechanism becomes irrelevant when $h = 0$ as Eq. (9) simplifies to the solvable homogeneous ODE: $uL'(u) = V(u)L(u)$. Then, the normalization condition $L(0) = 1$ imposes that $L(u) = q(u)/q(0)$, leading to $\beta = hL(a) = h/q(0)$. The abrupt loss of the delayed terms in Eq. (7) for $h = 0$ reveals the latter solution as a distinguished limit for L when $h \rightarrow 0$. In that respect, one can check that $h/q(0)$ is precisely the first-order term in Eq. (15) and reads explicitly

$$\beta = he^{\sum_j \beta_j w_j} + O(h^2) \quad \text{with} \quad w_j = \tau \int_0^a (e^{\mu_j v} - 1)/v dv, \quad (16)$$

where w_j is the effective synaptic weight of upstream neuron j . The nontrivial dependence of the effective weights w_j on the original synaptic strengths μ_j follows from including finite-size effects in the RMF framework [30, 44]. For small synaptic weights $\mu_j \ll 1/a$, we recover the classical mean-field regime for which the linear scaling $w_j \simeq \tau \mu_j a$ holds. We will later see that even for moderate values of μ_j , finite-size effects can have a substantial impact on evaluating the stationary moments of the dynamics.

Eq. (16) reveals that any nonlinear correction to the first-order estimate is due to including the reset mechanism. For Eq. (15) being a singular expansion, these higher-order corrections do not always yield a convergent series. However, we expect the first-order term to be a valid approximation as long as the reset timescale,

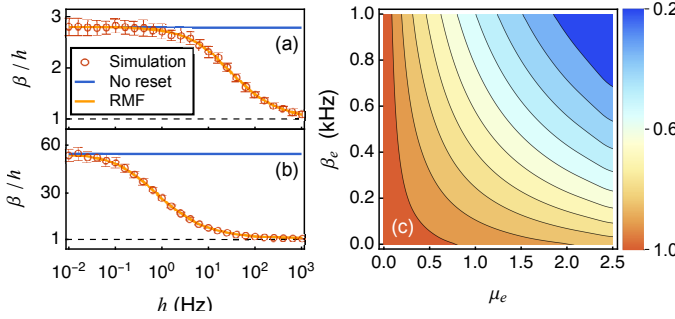


FIG. 4. **Nonlinearity of firing rate with the presence of reset.** In panel (a, b), the log-linear plots of β/h v.s. h show the non-linearity resulted from the post-spiking reset mechanism. Simulated rates are calculated over 400 spiking events and the values of standard deviation are calculated over 32 trials. In panel (a), the neuron is subjected to a single excitatory input with $\beta_e = 1$ kHz and $\mu_e = 1$, while in panel (b), the input is of $\beta_e = 1.5$ kHz and $\mu_e = 2.5$. Panel (c) is the contour plot of $\beta\tau$ at mid-point $h_{1/2}$, where excitatory input rate β_e and strength μ_e are varied. The contours are equidistant with respect to the value of $\beta\tau$. Parameters: $a = 0.1$, $\tau = 10$ ms.

i.e., the mean interspike interval $1/\beta$, remains large compared with the relaxation time τ : $\tau \ll 1/\beta$. This is because in this regime, fast relaxation erases the slower influence of the reset mechanism in shaping the distribution of the internal variable x . By contrast, in the regime of moderately large excitation $1/\beta \simeq \tau$, the reset mechanism starts to significantly impact the dynamics of x and to dampen the first-order exponential dependence of β on the input rates β_j . In principle, neurons can fire at a rate up to 200Hz for a leak time constant τ larger than 10ms. Thus, if one interprets the internal variable x as a proxy for the membrane voltage, the biophysically relevant range of neural activity includes values in the intermediary regime $\beta\tau \simeq 1$, for which nonlinear corrections are necessary. Exploring this regime requires using the Padé approximants associated to the divergent series.

We confirm numerically the above discussion by considering the simplest excitatory neuronal model, whereby a neuron is subjected to an input of rate β_e via the positive synaptic weight μ_e . Fig. 4(a, b) quantifies nonlinear corrections to the first-order prediction by plotting β/h as a function of h at fixed input conditions. As expected, the no-reset limit $\beta = h/q(0)$ holds for $h \rightarrow 0$. By contrast, in the opposite limit $h \rightarrow \infty$, the frequent resets due to spontaneous spiking erase the impacts of the relaxation as well as the inputs in between spikes, so that the spontaneous spiking emission dominates the dynamics: $\beta \rightarrow h$. By comparison with Fig. 4(a), Fig. 4(b) shows that the stronger excitatory drive, the larger the correction to the first-order terms. We mark the transition between the two asymptotic regimes by the mid-point $h_{1/2}$ such that $\beta(h_{1/2}) = h(1+1/q(0))/2$. To explore the domain of validity of the first-order expansion, we then check that at the mid-point value $h_{1/2}$, we have $\beta\tau \simeq 1$,

even for eventually large nonlinear correction. To this end, we perform a systematic RMF calculation to represent $\beta\tau$ for $h_{1/2}$ as a function of the input rate β_e and the synaptic weight μ_e . Fig. 4(c) shows that the stronger the input, the smaller value of $\beta\tau$. However, this dependence is weak and $\beta\tau \simeq 1$ holds throughout. This confirms our analysis about the domain of validity of the first-order approximation.

2. Moment analysis of the neuronal response

The crux of the RMF approach is to capture the stationary dynamics of a neuron via a parametric probabilistic model. Moreover, this model admits the output rate β as a sufficient statistics, assuming the biophysical parameters and the input rates known. This means that given these assumptions, all the moments of the stationary neuronal dynamics can be deduced from knowing β . For EGL neurons, the moments of interest are those of the stochastic intensity, $M_n(\lambda) = \mathbb{E}[\lambda^n]$, $n > 1$, and those of the internal variable x , $M_n(x) = \mathbb{E}[x^n]$, $n > 0$. With knowledge of β , $M_n(x)$ can also be computed efficiently for all $n > 0$ via expansions akin to Eq. (15) (see Appendix C). In turn, this allows one to estimate $M_n(\lambda)$, $n > 1$, by truncation of the series

$$M_n(\lambda) = h^n \sum_{k=0}^{\infty} \frac{(an)^k}{k!} M_k(x). \quad (17)$$

Here, we demonstrate that the above RMF computational framework accurately quantifies the response of EGL neurons subjected to Poissonian bombardments. We proceed by comparison with exact, event-driven, Monte-Carlo simulations under various driving conditions and for biophysically-relevant parameter values [31, 32] (see Appendix B). Bear in mind that in all cases, our computational results are obtained incomparably faster than those estimated via Monte-Carlo simulations. We will see that such a computational advantage leverages to neural networks in Sec. IV B 1. In demonstrating our point, we will discuss the general feature of the EGL neuronal response in light of the competition existing between the two timescales at play: the relaxation time τ , and the mean interspike interval $1/\beta$. We will also consider closed-form approximations for various regimes of activity.

For a feedforward neuron, the input-rate-dependence of β is encoded via the rate-transfer function Eq. (15). In Fig. 5, we explore this rate-transfer function numerically to reveal that—perhaps surprisingly—EGL neurons essentially behaves as stochastic rectifier linear units (ReLUs). In addition to our RMF calculation, we consider three types of approximations for comparison. At low spiking rate, the relaxation timescale dominates, e.g. $\tau \ll 1/\beta < 1/h$, and we utilize the first-order, no-reset approximation. At high spiking rate, e.g. $\tau \simeq 1/\beta$, we consider two heuristically-derived approximations in the

TMF limit and with or without relaxation. Both approximations are obtained via a simple probabilistic argument (see Appendix D).

In Fig. 5(a), when excitation dominates, the zero-order exponential approximation breaks down when β exceeds 10Hz, which happens at about 2kHz for the considered synaptic strength. Note that the input rates quantify the frequencies of synaptic activations so that 2kHz corresponds to, e.g., 20 upstream neurons firing at 100Hz or 200 upstream neurons firing at 10Hz. By contrast, RMF calculation accurately predicts the quasi-linear input-rate dependence of β (up to convergence failure). At high drive β_e , the output rate adjusts so that on average, the β_e/β received inputs are cancelled by a single reset over the timescale $1/\beta$. This balance generically leads to a weakly sublinear rate dependence in the RMF limit as well as in the TMF limit. In the TMF limit, we heuristically establish that at large β_e , $\beta_{\text{TMF}} \simeq a\beta_e\mu_e/\ln(1+a\beta_e\mu_e/h)$. This TMF approximation produces the right scaling but only becomes accurate for exceedingly high rates, when finite-size effects become negligible (see inset for the ratio β/β_{TMF}). Fig. 5(b) shows that the mean internal variable $\bar{x} = M_1(x)$ mirrors the behavior of β after logarithmic compression. A low-rate linear growth $\bar{x} \simeq \tau\beta_e\mu_e$ is followed by a logarithmic behavior $\bar{x} \simeq \ln(1+a\beta_e\mu_e/h)/(2a)$ at high drive. In Fig. 5(c-d), when inhibition dominates, the neuron seldom spikes so that $\tau \ll 1/\beta$, and the reset becomes irrelevant. Then, long interspike intervals allow for the integration of many inputs so that finite-size effect can be neglected as in the heuristic TMF limit. As a result, all approximations perform accurately.

Fig. 6 compares the second-moment predictions deduced from our various approximations. Comparing Fig. 6(a-b) and Fig. 6(c-d) consistently shows that predicting the variability in both λ and x requires RMF calculation when excitation dominates whereas the zero-order, no-reset approximation suffices when inhibition dominates (see Appendix D). Aside from this core observation, two remarks are worth making: First, we remark in Fig. 6(a-b) that the RMF calculation interpolates well between the low-rate and high-rate variability regimes. When the input rate is low, the variability mainly comes from the relaxation as in the no-reset limit. When the neuron spikes more frequently in response to strong drive, the reset mechanism becomes the dominant source of variability. The latter can be captured asymptotically by the TMF limit. Second, we remark in Fig. 6(c-d) that the TMF approximations fails to capture neural variability for both quantities, even though the mean response is accurately predicted in the inhibitory case. This is because TMF inherently neglect finite-size effects by assuming that the stochastic intensity varies deterministically in between spikes. Such an assumption leads to drastic underestimation of the variability in the inhibition-dominated regime, at least before the neuron becomes virtually silent.

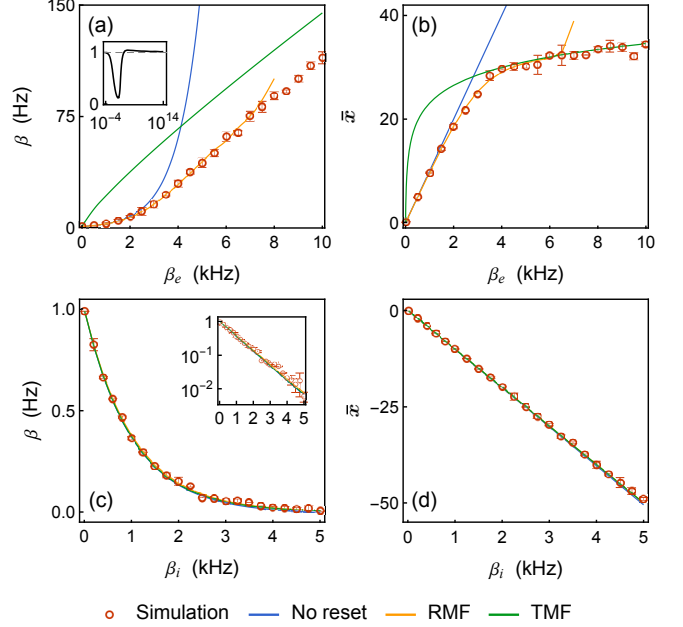


FIG. 5. **Input/output transfer function: mean neuron spiking rate β and mean internal variable \bar{x} .** For panel (a) and (b), the neuron is subjected to an excitatory input with varying rates β_e from 0 to 10 kHz and fixed strength $\mu_e = 1.0$. In panel (a), the top-left inset shows the ratio β/β_{TMF} in a wider range of input rates. For panel (c) and (d), the neuron is subjected to an inhibitory input with varying rates β_i from 0 to 5 kHz and fixed strength $\mu_i = -1.0$. The inset in panel (c) is plotted in logarithmic scale to show its exponential dependence. Parameters: $h = 1 \text{ Hz}$, $a = 0.1$, $\tau = 10 \text{ ms}$.

3. Finite-size effects and balanced regime

As mentioned above, a benefit of the RMF framework is that it enables the study of finite-size effects. In TMF approximations, finite-size effects are erased in the process of scaling interactions in the limit of infinite-size networks. As a result of this process, synaptic weights only appear as multipliers of the input rates in the rate-transfer functions [25]. This is not the case in RMF limits as shown by the nontrivial dependence of the effective weights w_j , which act as rate multipliers, on the original weight μ_j in Eq. (16).

We quantify these finite-size effects by elucidating the dependence of the mean and variance of the EGL neuronal response on the synaptic weights at fixed overall mean drive. By this, we mean that we jointly vary the numbers K_e, K_i and the weights μ_e, μ_i of the synapses so as to maintain the overall levels of excitation and inhibition, denoted by $E = K_e\mu_e$ and $I = K_i\mu_i$. Specifically, we compare the three following RMF approximations with their TMF counterparts: (1) K_e excitatory inputs alone; (2) K_i inhibitory inputs alone; (3) K_e excitatory inputs balanced by K_i inhibitory inputs with $K_e = K_i$ and $E = I$. The latter balance condition is a core assumption to a broad class of models account-

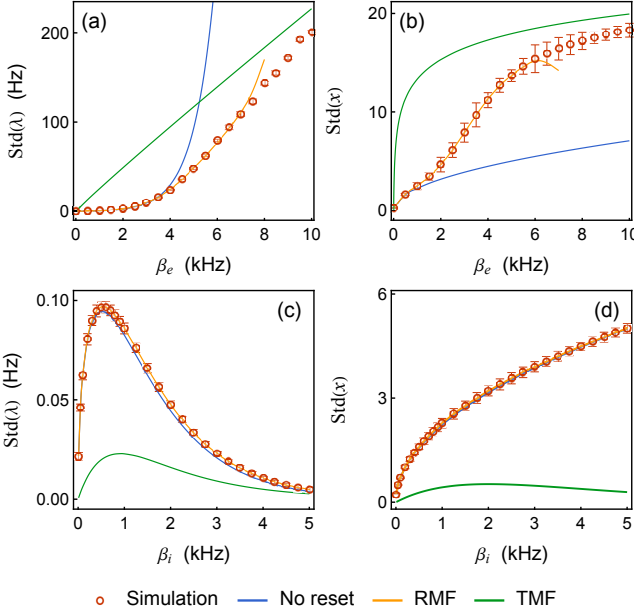


FIG. 6. **Input/output transfer function: standard deviation of the neuron spiking rate $Std(\lambda)$ and of the internal variable $Std(x)$.** For panel (a) and (b), the neuron is subjected to an excitatory input with varying rates β_e from 0 to 10 kHz and fixed strength $\mu_e = 1.0$. For panel (c) and (d), the neuron is subjected to an inhibitory input with varying rates β_i from 0 to 5 kHz and fixed strength $\mu_i = -1.0$. Parameters: $h = 1$ Hz, $a = 0.1$, $\tau = 10$ ms.

ing for the maintenance of neural variability in the limit of infinite-size networks, the so-called balanced network models [54].

Fig. 7 shows the RMF calculations and the simulated values for the mean and standard deviation of the internal variable with biologically relevant parameters. In all cases, our RMF predictions coincide with simulated results to numerical error. As expected for excitatory inputs (Fig. 7(a, a')), the input variability tends to average out for large number of inputs K_e . Accordingly, we observe that the TMF limit is accurate in this regime. By contrast, when K_e is small and finite-size effects are no longer negligible, the TMF limit marginally overestimates the mean, while underestimating the standard deviation by about twofold when $K_e = 7$. This is consistent with the TMF limit erasing variability, even in the presence of a stochastic reset. When driven by purely inhibitory inputs (Fig. 7(b, b')), neurons remain silent for long period over which the variability in the inputs averages out. As a result, the TMF limit performs well for all input number K_i . Nevertheless, the neural variability is still largely underestimated. This is again because TMF generally erases input variability, with a more drastic effect with inhibitory inputs. For instance, the TMF limit yields a seventeenfold reduction of the variability for $K_i = 7$. The overperformance of RMF over TMF is magnified in the balanced case (Fig. 7(c, c')). Under this condition, the TMF limit gives zero

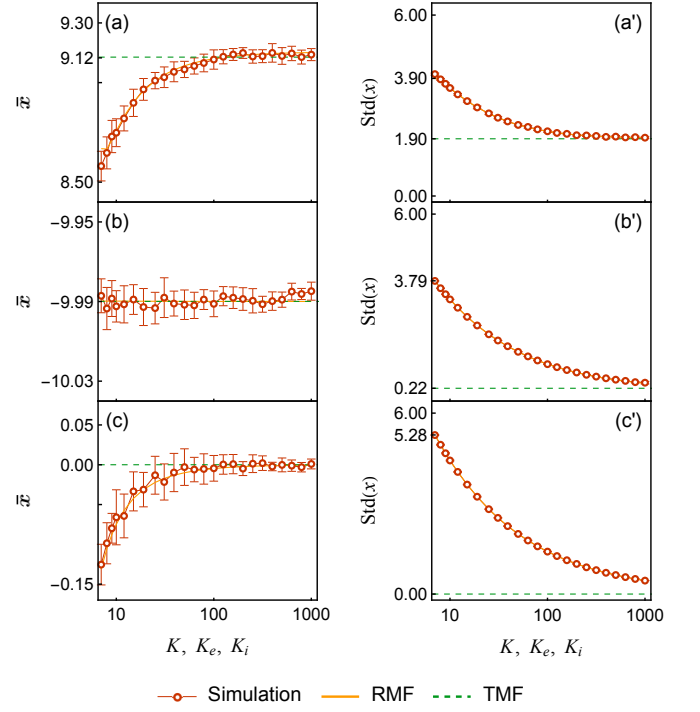


FIG. 7. **Finite-size effect.** Firing rates of a neuron subjected to different configurations of input, varying the number of input channels. For all panels, $E = 20$ and $I = -20$, $\mu_e = E/K_e$, $\mu_i = I/K_i$. Panel (a): excitation only, $\beta_e = 50$ Hz. Panel (b): inhibition only, $\beta_i = 50$ Hz. Panel (c): $K_e = K_i = K$, $\beta_e = \beta_i = 50$ Hz. Parameters: $a = \ln(100)/20 \approx 0.23$, $h = 1$ Hz, $\tau = 10$ ms.

mean and variance for the internal variable as there is no net drive: $\sum_j \beta_j \mu_j = 0$. However, the corresponding finite-size system is dominated by the next order fluctuation, yielding nonzero mean and variability. Actually, one can check that for balanced conditions, the mean firing rate increases in keeping with the standard deviation of x , and against the mean of x , as $K_e = K_i$ decreases. This confirms that the neural response is dominated by input variability in this regime. The slight negative trend of the mean of x is due to the nonlinearity of the exponential function, which biases against upward excursions from zero.

B. Metastability in the RMF limit

1. Network activity via fixed-point resolution scheme

We are now in a position to characterize the dynamics of a recurrent EGL network in the RMF limits. Recall that such limit dynamics are approximate versions of the original K -neuron dynamics, which are obtained via randomization of interactions across an infinite number of replicas. As a result of this randomization, within each replica, each neuron i experiences inputs as if delivered according to independent Poisson processes with

rate β_j , $j \neq i$. The parametrization of the inputs via rates alone is the root cause for the RMF frameworks being computationally tractable. Within a recurrent network, these rates need to be determined by solving the system Eq. (15) for self-consistent stationary rates $\beta = \{\beta_1, \dots, \beta_K\}$. By virtue of its interpretation in terms a physical limit, the RMF system Eq. (15) must admit solutions β^* . These solutions can be computed efficiently for EGL networks.

As a fixed-point system Eq. (15), it is natural to estimate possible solutions β^* via the naive iterative scheme: $\beta_{n+1} = \mathcal{F}(\beta_n)$. Aside from issues of Padé convergence, we expect this the naive scheme is locally convergent because the rate-transfer functions are weakly sublinear for large rates, which precludes runaway iterations. At the same time, these rate-transfer functions are also strongly supralinear (exponential) at low rate, so that solution uniqueness is guaranteed. In practice, we find that whenever the Padé approximants summation converges, the naive scheme always locally converges toward a solution $\beta_n \rightarrow \beta^*$, which may depend on the initial condition β_0 . A good choice for the initial condition is of the form $\beta_0 = h + \epsilon$ where ϵ represents a possibly random, perturbation. Such initial conditions can be made to fall into the region of Padé convergence, while it is possible to achieve distinct solutions by tuning ϵ , when several solutions exist. We compare the RMF and simulated rates for two network structures with strong, sparse connections: In Fig. 8(a, b), the considered network has a dominant feedforward structure, which promotes input independence as in the RMF limit. Accordingly, RMF rate approximations yield accurate predictions. In Fig. 8(c, d), the considered network has a fully recurrent networks, which promotes input correlations in excitatory networks. However, recurrent inhibition appears to maintain input independence and RMF calculation is accurate as well.

The two networks considered above have a single fixed-point RMF solution β^* . Intuitively, this is because the original system has a single “equilibrium” state, so that the corresponding ergodic dynamics is dominated by a single relaxation time. By contrast, metastable systems admits several local “pseudo-equilibria”, leading to multi-timescale dynamics: At small timescales, the dynamics is dominated by the relaxation time to the pseudo-equilibrium it occupies. At large timescales, the dynamics is dominated by sharp transition between distinct pseudo-equilibria. In the TMF approach, the rate of transitions between pseudo-equilibria vanishes exponentially fast with the size of the system, and the system becomes multistable in the infinite-size limit [55]. We expect a similar picture in the RMF approach. To validate this expectation, we consider the RMF limit for the simplest metastable dynamics, that of a neural-network model alternating between only two pseudo-equilibria. We expect to detect multistability via a transition whereby the RMF systems Eq. (15) start admitting several solutions. In practice, the stability of a solu-

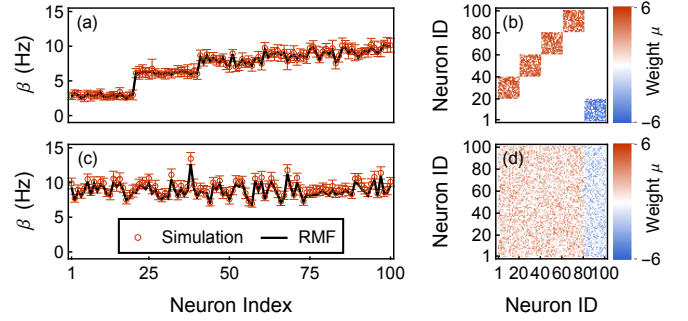


FIG. 8. **Comparison of RMF and simulated rates in inhomogeneous networks.** Two networks of 80 excitatory and 20 inhibitory neurons are considered. In panel (a), the network is feedforward with 4 excitatory layers and one last inhibitory layer inhibiting the first layer. The neurons between layers are connected with probability 75% and the synaptic strengths are uniformly random between 3 and 6, as shown in (b). Panel (c-d) are for a network with no particular structure. Each pair of neurons is connected with probability 50% and the synaptic strengths are uniformly random between 0 and 4. Parameters: $a = 0.1$, $h = 5$ Hz, $\tau = 10$ ms.

tion can be checked by creating an ensemble of iterations starting from randomized initial values.

2. Multistable limit of metastable networks

In principle, elementary computations can unfold in neural circuits by allowing some inputs to gate transitions between distinct output states of the circuit. In noisy neural networks, such gating processes give rise to metastable dynamics [11, 56–58]. Metastability has been studied for neural networks in the TMF limits [55, 59]. Here, we extend the analysis of metastability to the RMF framework with of focus on neural variability. Specifically, we demonstrate that our computational approach can capture the bistable response of a model neural network used to emulate perceptual rivalry [33].

The structure of the network is shown schematically in Fig. 9(a). The network comprises two symmetric groups of neurons Group_1 and Group_2 , with identical features and symmetric connections. Each group comprises a cluster of excitatory neurons ($\text{Exc}_{1,2}$) and a cluster of inhibitory neurons ($\text{Inh}_{1,2}$). The excitatory neurons in $\text{Exc}_{1,2}$ are fully connected within their own clusters, represented by the self-pointing arrows. The inter-cluster arrows represent full connection between corresponding clusters. For simplicity, we set all the excitatory and inhibitory synaptic strengths to be equal to μ_e and μ_i , respectively. Aside from their within network interactions, all neurons are subjected to TMF-type inputs of fixed rates and strength with $(\beta\mu)_{\text{TMF}} = 1.5$ kHz. This corresponds, for instance, to each neuron having 1000 weak synapses of strength $\mu_{\text{TMF}} = 0.1$ activating at a rate of $\beta_{\text{TMF}} = 15$ Hz. Accounting for these TMF-type inputs amounts to adding a linear term in the function

$V(u) \rightarrow V(u) + (\beta\mu)_{\text{TMFU}}$. This hybrid picture is biologically relevant following the evidences that neurons receive background signals from a large number of background synapses and that only a few key components dictate the behaviors of the system [23, 24]. The inclusion of strong mutual inhibition across symmetric groups of neuron shall turn the network into a stochastic bistable switch. In the following, we study such a switch for a small total number of neurons ($N = 40$ with 10 neurons in each cluster), so that neural variability will be a key determinant of the overall dynamics. The ability to deal with such small systems is one of the core benefits of the RMF framework.

We first confirm through simulations that this system can indeed exhibit bistability. Fig. 9(b-d) shows the traces of the internal variable x of one representative neuron in Exc_1 . In Fig. 9(b), we simulate with $\mu_e = 0.7$ and $\mu_i = -4.0$. In this case, all activities are strongly suppressed by the inhibition. The system exhibits no bistability. Upon increasing the excitatory strength to $\mu_e = 1.2$ while leaving μ_i unchanged, the system becomes marginally bistable as shown by the enhanced fluctuations observed in Fig. 9(c). This is an indication that the corresponding deterministic system is on the edge of a dynamical transition or bifurcation. However, such bifurcation are notoriously difficult to detect in a noisy setting. Further increase of μ_e reveals clear alternations between two relatively stable states as shown in Fig. 9(d) for $\mu_e = 1.7$. We refer to these states as the “up” state or the “down” state depending on the mean value of x during these states. Fitting the simulated dynamics via hidden Markov Model allows us to parse out the various dominance periods during which either Group_1 or Group_2 is up [60, 61]. This assumes that conditionally to be up or down, the distribution of the internal variable x remains approximatively Gaussian and offers to compute distinct moments of the dynamics for up and down states.

Next, we check that our RMF framework can capture this bistable switch behavior, and perhaps even detect the bifurcation. To this end, we numerically solve the self-consistent rate Eq. (15) obtained in the RMF limit for the considered network. As expected, we find two distinct stable solutions for high enough cross-inhibition μ_i . When the RMF limit is multistable, different choices of initial values can lead to distinct solutions so that not surprisingly the choice of the initial values matters. We can control to which solutions the iteration scheme converges by choosing initial values in the basin of attraction of the desired solution. For instance, if we choose larger initial values for neurons in Group_1 (e.g., $\beta_{0,i} = h + \epsilon, i \in \text{Group}_1, \epsilon > 0$), the iteration will converge to a state where Group_1 is in the up state. The thus obtained two sets of rate solutions parametrize two probabilistic models for two up and down metastable states.

In Fig. 10(a-c), we compare exact simulation results in the finite-size network (data points) to our theoretical calculations in the infinite-size RMF limit (solid curves).

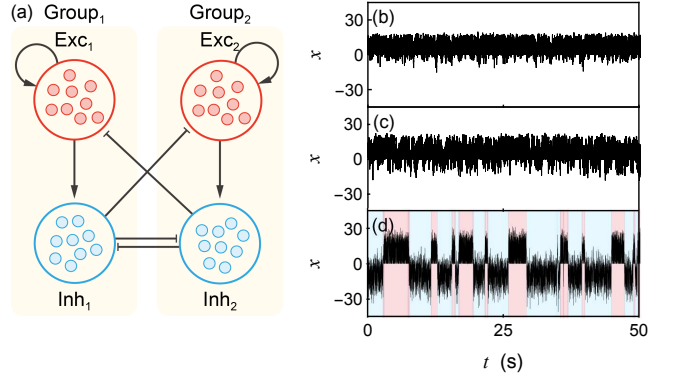


FIG. 9. Network structure and simulated traces of internal variable x . Panel (a): The system has two identical groups ($\text{Group}_{1,2}$) of neurons with symmetric connections. In each group, there is one cluster of excitatory neurons and one cluster of inhibitory neurons. Each cluster consists of $K/4$ neurons. The connections between clusters are as shown. The synaptic strength is μ_e from any excitatory neuron and μ_i from any inhibitory one. Panel (b-d): we plot the traces of x for a representative neuron in Exc_1 , with fixed inhibitory strength $\mu_i = -4.0$. The system exhibits: in panel (b), monostability with $\mu_e = 0.7$; in panel (c), fluctuation with $\mu_e = 1.2$; in panel (d), bistability with $\mu_e = 1.7$. Parameters: $K = 40, h = 1 \text{ Hz}, a = \ln(100)/20 \approx 0.23, \tau = 10 \text{ ms}$.

The branching behavior of $\beta = \mathbb{E}[\lambda], \mathbb{E}[x]$ and $\mathbb{E}[x^2]$ clearly indicates a transition from a monostable regime to a bistable regime. Our calculation is in good agreement with the simulated values outside of the shaded region. In the shaded region, where the bifurcation between monostability and bistability occurs, it is numerically ill-posed to distinguish between up and down states. The system does not persist in either states long enough for us to accurately compute the desired quantities. Fortunately, and as in the TMF limit, our theoretical calculation offers to precisely pinpoint the bifurcation via the forking behavior of the solution rates. However, contrary to the TMF limit, the RMF limit allows us to retain the neural variability due to stochastic inputs. In particular, at the cost of neglecting correlations, the RMF approach provides with estimates about the higher moments of the dynamics. For instance, Fig. 10(c) shows the simulated and theoretically calculated second moments $\mathbb{E}[x^2]$. The non-monotonic behavior of $\mathbb{E}[x^2]$ in excited state due to the change of sign is also captured. It is worth noting again that, although we erase the correlation among neurons in the RMF limits, the variability is well preserved. The absence of correlation in our model seems not to affect our prediction. This might be due to the cancelling effect of inhibition in the system as well as the fully connected subnetwork structure of our model [62].

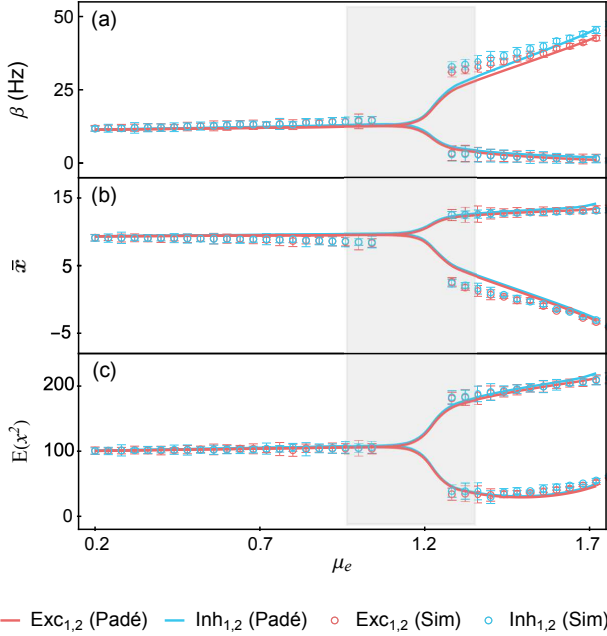


FIG. 10. Simulated and theoretically calculated quantities. These figures shows in panel **(a)**, the output rates β ; in panel **(b)**, the mean internal variables \bar{x} and in panel **(c)**, the second moments of x , with varying excitation strength μ_e and fixed inhibitory strength $\mu_i = -4.0$. For the simulated quantities shown in the figure, values within a cluster are averaged to generate one data point. Gray-shaded region is where the transition from monostable system to bistable system happens and we are not able to compute the simulated rates accurately, however, we can still perform RMF calculation within this region. Parameters: $K_{\text{total}} = 40$, $h = 1 \text{ Hz}$, $a = \ln(100)/20 \approx 0.23$, $\tau = 10 \text{ ms}$.

3. Finite-size effects and metastability

Synaptic distributions in real neural networks follow a highly skewed distribution: there is a large number of weak connections but only a few strong ones, whose strengths vary over two orders of magnitudes [63]. Studies have also shown that meaningful neural activity is triggered by strong, correlated synaptic inputs rather than uncorrelated, weak ones [23, 24]. Our RMF modeling approach allows us to quantify how the size of the synaptic inputs impacts bistability, at the cost of neglecting activity correlations. To do so, we consider the same hybrid model where neurons are all subjected to TMF-type background inputs, but where the circuit connections implementing cross-inhibition are treated in the RMF limits.

In this setting, we can quantify the emergence of bistability when varying the synaptic strength μ_e and μ_i involved in the cross-inhibitory circuit, thereby performing a phase space analysis of the network. Importantly, this phase space analysis only requires solving the corresponding self-consistent RMF equations rather than prohibitively costly simulations. We utilize the RMF solu-

tion rates to quantify bistability via the following bifurcation observable Δ :

$$\Delta = \frac{\beta_{\text{Exc}_u} + \beta_{\text{Inh}_u} - \beta_{\text{Exc}_d} - \beta_{\text{Inh}_d}}{\beta_{\text{Exc}_u} + \beta_{\text{Inh}_u} + \beta_{\text{Exc}_d} + \beta_{\text{Inh}_d}}. \quad (18)$$

where the subscripts Exc_u , Inh_u and Exc_d , Inh_d refer to neuronal groups in the up and down states, respectively. By definition, as both excitation and inhibition are larger in the up state, the observable Δ ranges between 0 and 1. In the monostable regime, $\Delta \approx 0$ is minimum since $(\beta_{\text{Exc}_u}, \beta_{\text{Inh}_u}) \approx (\beta_{\text{Exc}_d}, \beta_{\text{Inh}_d})$. By contrast, in the bistable regime, when the neurons are silenced when in the down state, i.e. $(\beta_{\text{Exc}_d}, \beta_{\text{Inh}_d}) \approx (0, 0)$, $\Delta \approx 1$ is maximum. Fig. 11(a) shows the parametric density plot of Δ obtained by varying μ_e and μ_i .

As expected, the regime of activity of the system is controlled by the overall level of cross-inhibition, which appears loosely linear in μ_e and μ_i . This is because cross-inhibition obviously requires excitation of the mediating inhibitory neurons. For weak cross-inhibition, the network response is dominated by the uniform TMF background and fluctuates around its only equilibrium state. Increasing μ_e and μ_i leads to a sharp transition to a bistable regime. For small circuits, with about 10 neurons per subnetworks, this transition occurs for large synaptic weights requiring a RMF treatment as the TMF approximation yields wrong rate estimates. The sharpness of the transition indicates a strong silencing of neurons in the down state, in line with the strong nonlinearity of the network dynamics. In that respect, we find that the TMF approximation predicts that bistability emerges for smaller synaptic weights than observed in small networks, while also underestimating the firing rates.

We conclude by utilizing our RMF computational approach to exhibit behaviors that are otherwise challenging to obtain via simulations. Specifically, we exhibit in Fig. 11(b) the scaling of the critical weights at the bifurcation μ_e with respect to the subnetwork size K , assuming a fixed ratio $\mu_e/\mu_i = 0.2$ and $\mu_e/\mu_{\text{TMF}} = 10$. Interestingly, we found that the critical weight scales approximately as $1/\sqrt{K}$, similar to the scaling formally defining the balanced thermodynamic limit. In this limit, inhibition and excitation cancel one another on average. As a result, neuronal activity is driven by the fluctuations in the inputs. The $1/\sqrt{K}$ scaling ensures that neural variability is preserved in the large K limits for independent inputs. We observe a similar phenomenon for critically tuned networks in the RMF limit, for which inputs are always independent. This is because neural variability is an invariant of the dynamics at the bifurcation, where networks start alternating between the newly individualized up and down states. Preserving this variability throughout network sizes in the RMF limit naturally requires a $1/\sqrt{K}$ scaling, which remarkably persists down to very small system sizes.

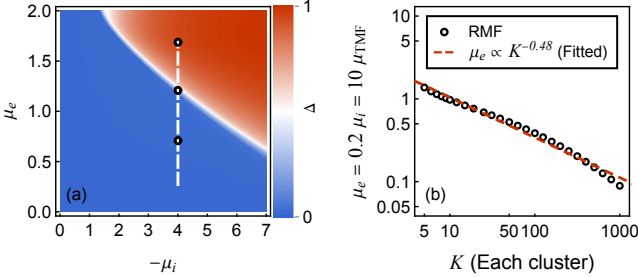


FIG. 11. **Phase transition.** Panel (a): In this density plot of bifurcation observable Δ , μ_e and μ_i are varied. The white dashed line represents the parameters $(\mu_e, -\mu_i)$ used in Fig. 10. The black circles correspond to the parameters for the simulations shown in Fig. 9(b-d). Panel (b) is the log-log plot of the value of μ_e at the onset of bifurcation varying the size of the network, determined by thresholding $\Delta = 0.01$ in the RMF calculation (black dots). The red dashed line is the linear fitting in the log-log scale, which has a slope of -0.48 . Parameters: $h = 1 \text{ Hz}$, $a = \ln(100)/20 \approx 0.23$, $\tau = 10 \text{ ms}$.

V. DISCUSSION

A. Modeling assumptions for a computational framework

One of our leading motivation is the hope to quantify finite-size effects in the dynamics of noisy neural network. To this end, we have adopted a reductionist modeling approach building on the central assumptions that noise arises internally via rate-based, spike-generating process. To account for the potential individual impact of a single synaptic activation, we have modeled the instantaneous spiking rate as a history-dependent stochastic intensity λ . Each synaptic delivery transiently impacts this stochastic intensity by causing instantaneous jumps in keeping with the synaptic weights. This bare framework leads to a series of well-identified pitfalls, which can be fixed with additional modeling components.

First, the requirement that the stochastic intensity remains a nonnegative quantity imposes that the joint integration of inhibition and excitation should be mediated by an internal variable x . This variable, albeit thought of as a membrane potential, is allowed to vary without bound, so that inhibition and excitation can be safely integrated algebraically. In turn, the stochastic intensity is deduced from x via a necessarily nonlinear, rectifying function, akin to the $f - I$ curves. The simplest such function that is also monotonic is the exponential one [17, 64].

Second, with supralinear rectifying functions, the dynamics of recurrent networks can become ill-posed, with possibly diverging stochastic intensities [65]. Such an explosive behavior can be tamed by introducing an additional nonlinearity in the rectifying functions, e.g., by imposing biologically plausible high-rate saturation. An alternative route that does not require saturation is to consider an instantaneous post-spiking reset mechanism,

which implements a form of refractory period [41, 42]. By contrast with that implied by saturation, the type of nonlinearity introduced by this reset mechanism is still computationally tractable.

Third, in the absence of relaxation, neuronal dynamics may be ill-posed when neurons are dominated by inhibitory inputs, even in the presence of a reset mechanism. Indeed, steady inhibition can cause the internal variable to diverge over time $\lim_{t \rightarrow \infty} x(t) = -\infty$, effectively silencing the neuron. We remedy such a caveat by allowing the internal variable to relax toward a base level. While biophysically relevant, such relaxation precludes runaway dynamics, and thereby neuronal silencing. Incidentally, it also guarantees the ergodicity of the finite-size dynamics [25].

B. Biophysical relevance and limitations

Theoretical considerations alone show all the above three components must be included in any stochastic-intensity-based neural models. These are also the only modeling features we consider. This drastic oversimplification clearly neglects important aspects of neuronal processing such as propagation delays [66], synaptic adaptation and fatigue [67], or neuronal compartmentalization [68]. Perhaps the most serious limitation of EGL model is being current-based for integrating inputs without conductance mediation. In conductance-based models, the internal variable x explicitly models the membrane voltage, which is naturally bounded by the ionic reversal potentials. This naturally excludes the possibility of rate explosion. That being said, our point here is to develop a computational framework where the impact of finite-size effects can be quantified in relation to a few key modeling assumptions.

Despite the crudeness of their modeling assumptions, we found that EGL neurons operate in a biologically relevant regime for parameters inferred from real-world measurements. In particular, we set large synaptic weights to be such that a single synaptic excitation at base level causes the internal variable x to transiently increase by 2% of its range. Here we defined the range as the mean value of x when $\beta \simeq 100 \text{ Hz}$. Such choices mirror the observation that large synaptic events cause up to $\sim 0.5 \text{ mV}$ depolarization at the soma, for a typical upward voltage range of 20 mV . There are also natural choices for the two timescales featuring as free parameters [64]: We set the relaxation timescale τ to be equal to the membrane time constant 10 ms . We adopted a base rate of $h = 1 \text{ Hz}$, as the putative spontaneous firing rate of an isolated neuron. The latter choice of a base rate is actually more flexible than it appears. Indeed, varying levels of background activity modulates the effective value of h .

There are direct extensions to EGL models that can be treated within our framework. One alteration is to implement a post-spiking hyperpolarization of fixed size, say ν , rather than a hard reset to zero. In this case,

the discrete derivative term shall be replaced by the delay term $L(a + u)(e^{u\nu} - 1)/u$, and the resulting DDEs is still tractable via resolvent formalism. However, the rate-transfer function would become asymptotically linear so that network dynamics will no longer be unconditionally stable. Other alterations are to allow for relaxation toward a value $b \neq 0$ and resets to value $r \neq 0$. This leads to considering auxiliary terms of the form $V(u) = bu + \sum_j \beta_j(e^{u\mu_j} - 1)$ with spontaneous rate of the form he^{ar} . Again, the resulting RMF problems are still tractable but now offers some interesting modeling perspective. One such perspective is to allow for b and r to be slowly dependent on neuronal activity to model some form a fatigue or adaptation process.

C. Analyticity, nonlocality, and singular perturbation

The computational framework of the RMF approach relies on the Poisson hypothesis, which posits that neural inputs are distributed according to independent Poisson processes [30, 45]. Such an hypothesis is justified when neuronal interactions are randomized across an infinite number of replicas of a given finite-size networks. The simplifying Poisson hypothesis allows one to parametrize the probability distribution of a neural networks via the individual neuronal spiking rates alone. Therefore, in the RMF limit, elucidating the typical state of a neural network amounts to solving self-consistently for these stationary firing rates. These rates are determined as fixed-point solutions of the system of equations specified by rate-transfer relations, which can be seen as implementing some nonconservative Kirchhoff's laws [69].

To compute rate-transfer functions in the RMF limit, our strategy is to use conservation laws holding in the stationary regime to functionally characterize the typical distribution of neuronal states via their MGFs. For EGL neurons, such a functional characterization takes the form of nonlocal DDEs bearing on the MGFs L . Analytical solutions to these DDEs uniquely specify these MGFs, from which the stationary rates can be deduced as $\beta = hL(a)$. However, as for most nonlocal equations, solutions to our DDEs cannot be expressed explicitly and one has to resort to singular perturbative methods.

In principle, one can hope to obtain tractable distinguished limits in two asymptotic regimes: for vanishing relaxation $\tau \rightarrow \infty$ and for vanishing spontaneous rate $h \rightarrow 0$. In practice, only the limit $h \rightarrow 0$ is useful. Indeed, when $\tau \rightarrow \infty$, the DDE simplifies to a pure delay equation, whose analytic solutions are not known in closed form. More fundamentally, in the absence of relaxation, we do not know whether the original dynamics is ergodic. In particular, the RMF limit may become ill-posed with neurons being silenced for diverging durations by increasingly large amounts of inhibition. By contrast, when $h \rightarrow 0$, the DDE becomes a simple ODE, so that the corresponding MGF $L_{h=0}$ is given as the only solu-

tion satisfying the normalization condition $L_{h=0}(u) = 1$. This solution is valid whenever the reset mechanism can be neglected, i.e., for low output spiking rate $\beta \ll 1/\tau$.

For moderately large firing rates, we are able to solve the DDEs via resolvent formalism. Interestingly, this resolution does away with the requirement of specifying initial conditions on a delayed interval, as one generally expects for DDEs. This is because the resolvent formalism naturally selects for the set of solutions such that the graph of $(h, u) \mapsto (h, L(h, u))$ forms a continuous manifold anchored on the analytical boundary $L_{h=0}$ when $h \rightarrow 0$. Thus, we circumvent the need for local initial conditions over an interval for L_h at fixed h , by imposing global regular conditions on $(h, u) \mapsto (h, L(h, u))$ when varying h . We conjecture that this manifold is analytic in u as required for MGF functions, whereas analyticity in h can fail, at least in $h = 0$ when excitation dominates the input drives. Because of the lack of analyticity in h , the resolvent formalism only produces a formal, possibly divergent, series expansion in terms of powers of h , the singular perturbation parameter. Although we have not characterized the type of nonanalyticity at stake, we found that Padé approximants summation can accurately predict output rates when the formal series diverges. This suggests that $L(\cdot, u)$ might be a meromorphic function on some open region of the complex plane whose singularities all lie outside of the non-negative real axis [70].

D. Dynamical transition via RMF limits

We utilize our RMF framework to partially analyze the metastable dynamics of small networks. As well-known for the TMF limit, metastability turns into multistability in the RMF limit: the residence times in the various pseudo-equilibria diverge exponentially with the number of replicas. By contrast with the TMF limit however, these pseudo-equilibria remain probabilistic, with stationary distributions parametrized by self-consistent firing rates. The RMF approach predicts the transition to bistability in small metastable networks with accurate estimates of the mean activity as well as the neural variability, when conditioned to being in either pseudo-equilibrium.

Detecting bifurcation in stochastic systems is a notoriously arduous task [71]. This is because including noise in a finite-dimensional systems generally turns its dynamics into an infinite-dimensional one. For instance, one can show that the transient dynamics of RMF EGL network is such that the time-dependent MGF $L_i(t, u) = \mathbb{E}[e^{ux_i(t)}]$ satisfies the nonlocal partial differential equation

$$\begin{aligned} \partial_t L_i(t, u) + \frac{\partial_u L_i(t, u)}{\tau_i} - \frac{V_i(t, u)}{u} L_i(t, u) \\ + h_i \left(\frac{L_i(t, u + a_i) - L_i(t, a_i)}{u} \right) = 0, \end{aligned} \quad (19)$$

whose full resolution appears to resist direct analytic treatment. However, in the stationary regime, the infinite-dimensional PDE problem reduces to a DDE problem, which is revealed to be finite-dimensional via our RMF analysis. Solving for the stationary rates then shows that the transition to bistability occurs when the single low cross-inhibition equilibrium loses stability, as two new pseudo-equilibria emerge. Thus, the transition to bistability is dynamically akin to a classical, finite-dimensional supercritical pitchfork bifurcation.

Conceptually, the RMF framework allows us to probe a dynamical bifurcation as a static phase transition. In that regard, we predict that the emergence of bistability in the RMF limit is analogous to a continuous phase transition for the Curie-Weiss model in the absence of external field. Below a critical value for cross-inhibition, symmetric groups of neurons fluctuates around common equilibrium states, whereas above that critical value, one group of neurons will silence its symmetric counterpart. This corresponds to the emergence of low-temperature spontaneous magnetization in the Curie-Weiss. Our expectation is confirmed by the apparent continuity of the rates through criticality. However, the order of the phase transition in the RMF limit remains to be elucidated as numerics suggest a rather smooth dependence of the rates. Moreover, since neuronal correlations are destroyed in the RMF limit, such a phase transition is a purely dynamical phenomenon. That being said, critical RMF networks can still exhibit nontrivial correlations across replicas, but presumably with no direct relation to the original dynamics.

Despite its static approach, we hope to leverage our RMF framework to estimate key dynamical properties of metastable dynamics, such as the transition rates between pseudo-equilibria. In the classic theory of reaction rate, these transition rates can be approximated via phenomenological Arrhenius law given some notion of energy landscapes [72]. Unfortunately, we do not have a consistent notion of energy in our model since the spiking counts are not conservative. Nevertheless, we can still use the first and second moments of the internal variable x to form Arrhenius-type candidate laws for the observed rates. In this regard, preliminary analysis suggests that the rates scale exponentially with $\mathbb{E}[x_u]/\text{std}(x_u)$ where the subscript u's refers to the up state. This demonstrates that the static approach of the RMF framework is predictive of the transition rates. Further quantifying the dependencies of the transition rates on other modeling parameters will require a more principled treatment. Such treatment will extrapolate finite-size transition rates from the diverging scaling behavior of the corresponding rates in the RMF limit, which shall satisfy the large deviations principle [73].

ACKNOWLEDGMENTS

We acknowledge the support by the Provost's Graduate Excellence Fellowships at Colledge of Natural Science at University of Texas at Austin; grant from Center of Theoretical and Computational Neuroscience at University of Texas at Austin; and Alfred P. Sloan Research Fellowship FG-2017-9554. We would like to thank François Baccelli, Michel Davydov, Yiran Hu, Zhao Liu, Manyi Yim for insightful discussions.

Appendix A: Derivation of the DDEs

In Sec. II C of the main text, we claim the MGF L_i satisfies the DDE Eq. (7). We derive it here from the rate-conservation principle on the MGF Eq. (6):

$$\begin{aligned} e^{ux_i(t)} - e^{ux_i(0)} &= -\frac{u}{\tau_i} \int_0^t x_i(s) e^{ux_i(s)} ds \\ &\quad + \sum_{j \neq i} (e^{u\mu_{ji}} - 1) \int_0^t e^{ux_i(s^-)} P_j(ds) \\ &\quad + \int_0^t (1 - e^{ux_i(s^-)}) N_i(ds), \end{aligned} \quad (6)$$

First, we take the expectation value on both sides and the L.H.S. becomes zero in stationary limit:

$$\begin{aligned} 0 &= -\frac{u}{\tau_i} \mathbb{E} \left[\int_0^t x_i(s) e^{ux_i(s)} ds \right] \\ &\quad + \sum_{j \neq i} (e^{u\mu_{ji}} - 1) \mathbb{E} \left[\int_0^t e^{ux_i(s^-)} P_j(ds) \right] \\ &\quad + \mathbb{E} \left[\int_0^t (1 - e^{ux_i(s^-)}) N_i(ds) \right]. \end{aligned} \quad (A1)$$

The first term is an ordinary integral and in stationary limit, it becomes

$$\begin{aligned} -\frac{u}{\tau_i} \mathbb{E} \left[\int_0^t x_i(s) e^{ux_i(s)} ds \right] &= -\frac{u}{\tau_i} t \mathbb{E} [x_i e^{ux_i}] \\ &= -\frac{u}{\tau_i} t L'_i(u). \end{aligned} \quad (A2)$$

The stochastic integrals in the second and third terms involving point processes can be handled using Palm calculus [47]. Palm calculus is established on Palm probability measure, which intuitively is the probability viewed from the event occurrence time of given point process. Here we state the key result from Palm calculus. For stationary process $X(t)$ with some mild conditions, the expectation of the integral on point process $N(t)$ of rate β has the following relation:

$$\mathbb{E} \left[\int_0^t X(s) N(ds) \right] = \beta t \mathbb{E}_N^0 [X(0^-)], \quad (A3)$$

where $\mathbb{E}_N^0[\cdot]$ denotes the expectation with respect to Palm probability. Further, if there is a stochastic intensity process $\lambda(t)$ associated with the point process $N(t)$, we have for arbitrary real-valued function f ,

$$\beta \mathbb{E}_N^0[f[X(0^-)]] = \mathbb{E}[f(X)\lambda]. \quad (\text{A4})$$

For the expectation in the sum of the second term, we use Eq. (A3) and it becomes

$$\begin{aligned} \mathbb{E}\left[\int_0^t e^{ux_i(s^-)} P_j(ds)\right] &= \beta_j t \mathbb{E}_{P_j}^0\left[e^{ux_i(0^-)}\right] \\ &= \beta_j t \mathbb{E}[e^{ux_i}] \\ &= \beta_j t L_i(u), \end{aligned} \quad (\text{A5})$$

where the second equality is because P_j is an independent process. For the last term, we use Eq. (A3) and Eq. (A4) successively and get

$$\begin{aligned} \mathbb{E}\left[\int_0^t (1 - e^{ux_i(s)}) N_i(ds)\right] &= \beta_i t \mathbb{E}_{N_i}^0\left[1 - e^{ux_i(0^-)}\right] \\ &= \beta_i t - \beta_i t \mathbb{E}_{N_i}^0\left[e^{ux_i(0^-)}\right] \\ &= \beta_i t - t \mathbb{E}[h_i e^{a_i x_i} e^{ux_i}] \\ &= \beta_i t - t h_i L_i(u + a). \end{aligned} \quad (\text{A6})$$

Now we can substitute Eq. (A2), Eq. (A5) and Eq. (A6) into Eq. (A1) and Eq. (7) will be recovered once canceling the common factor t .

Appendix B: Simulation method

In the main text, we compare the theoretical and simulated results of the EGL model throughout. The simulated results are obtained from an event driven method for simulating spiking neuron network [31, 32]. Here, we outline the procedure of this method.

For the exponential firing neuron with internal variable x , the time till next spike is distributed according to the following complementary cumulative distribution function (survival function):

$$\mathbb{P}(T > t) = \exp\left\{-\int_0^t h e^{axe^{-s/\tau}} ds\right\}. \quad (\text{B1})$$

When $x = 0$, the distribution $\text{Neuron}(\tau, h, a, x)$ reduces to $\text{Exp}(h)$. When $x \neq 0$, we can integrate Eq. (B1) and obtain explicitly

$$\mathbb{P}(T > t) = \exp\left\{h\tau \left[\text{Ei}(axe^{-t/\tau}) - \text{Ei}(ax)\right]\right\}, \quad (\text{B2})$$

where $\text{Ei}(x) = -\int_{-x}^{\infty} e^{-t}/t dt$ is the exponential integral function. Then we apply inverse transform sampling technique by sampling $u \sim \text{Uniform}(0, 1)$ and solving $\mathbb{P}(T > t) = u$ for t . Using the fact that $\text{Ei}(x) = \text{li}(e^x)$, where $\text{li}(\cdot)$ is the logarithmic integral function, we have

$$t = -\tau \ln\left\{\frac{1}{ax} \ln\left[\text{li}^{-1}\left(\text{Ei}(ax) + \frac{1}{h\tau} \ln u\right)\right]\right\}. \quad (\text{B3})$$

Note that the branch of $\text{li}(\cdot)$ function should be determined by the sign of x : when $x < 0$, we choose the left branch and when $x > 0$, we choose the right branch.

At each iteration step, we sample a random number t representing waiting time till the next event for each neuron. Among all sampled waiting time: $t_{\text{neuron},1}, t_{\text{neuron},2}, \dots$, we choose the smallest one as the time of occurrence of the next event. Suppose this event has waiting time t_{next} . For all the neurons, we multiply an exponential relaxation factor $e^{-t_{\text{next}}/\tau}$ to the internal variables. Then, for all the neurons that are connected to the source neuron of this event, we add the corresponding connection strength to the internal variables. Namely,

$$x_i \leftarrow x_i e^{-t_{\text{next}}/\tau} + \mu_{\text{source} \rightarrow i}. \quad (\text{B4})$$

We collect all necessary information at each iterative step and repeat this process until certain criteria are satisfied (event counts, simulated time, etc.).

Appendix C: Calculation for higher moments

In Sec. IV of the main text, we compute the second moments of the intensity λ and internal variable x of our model. The preservation of higher moments is one of the benefits of our model. In fact, we can compute the moments of arbitrary orders, which we formulate here.

Recall that the moments of λ and x are related by Eq. (17) in EGL models:

$$M_n(\lambda) = h^n \sum_{k=0}^{\infty} \frac{(an)^k}{k!} M_k(x). \quad (\text{17})$$

We formulate the equations for the higher moments of x and those of λ can be computed by using truncated Eq. (17). From the MGF $L(u) = \mathbb{E}[e^{ux}]$, the moments of x can be written as $M_k(x) = L^{(k)}(0)$. Since $H(u) = (L(u + a) - L(a))/u$ and H has the following series expansion

$$H(u) = \frac{\beta}{h} \sum_{m=0}^{\infty} (-h\tau)^m Q_m(u), \quad (\text{13})$$

we arrive at

$$M_k(x) = [uH(u)]^{(k)} \Big|_{u=-a} = \frac{\beta}{h} \sum_{m=0}^{\infty} (-h\tau)^m [uQ_m(u)]^{(k)} \Big|_{u=-a}. \quad (\text{C1})$$

Eq. (C1) is valid for $k \geq 1$ and can be computed using Padé approximants summation in a similar fashion.

Appendix D: Different approximation methods

In Sec. IV A, we compare our theoretical calculation with the no-reset approximation and TMF approximations. Here, we summarize these different approximation methods.

1. No post-spiking reset (low rate approximation)

When the input rate is low, the neuron integrates the received inputs slowly and also spikes sparsely. The neuron relaxes on a faster time scale and prevents the internal variable from going to infinity and the reset mechanism does not play significant roles. In this case, Eq. (7) reduces to the ODE $uL'(u) = \tau V(u)L(u)$. With the normalization condition $L(0) = 1$ we can solve $L(u) = q(u)/q(0)$, where $q(u) = \exp(\tau \int_a^u V(v)/v dv)$.

The n -th moment of the intensity λ is given by

$$\mathbb{E}[\lambda^n] = h^n L(ka) = h^n \frac{q(na)}{q(0)}. \quad (\text{D1})$$

Specifically, the mean and variance of λ are

$$\mathbb{E}[\lambda] = \frac{h}{q(0)}, \quad \mathbb{V}[\lambda] = \frac{h^2}{q^2(0)} [q(2a)q(0) - 1]. \quad (\text{D2})$$

The k -th cumulant ($k \geq 1$) of x can be calculated:

$$\kappa_k = [\ln(L(0))]^{(k)} = \frac{1}{k} V^{(k)}(0) = \frac{\tau}{k} \sum_{\text{input } j} \beta_j \mu_j^k. \quad (\text{D3})$$

Specifically, the mean and variance of x are

$$\mathbb{E}[x] = \tau \sum_{\text{input } j} \beta_j \mu_j, \quad \mathbb{V}[x] = \frac{\tau}{2} \sum_{\text{input } j} \beta_j \mu_j^2. \quad (\text{D4})$$

2. TMF limits without relaxation

In the TMF limits, the neuron receives infinitesimal signal deliveries from infinitely many inputs. Thus, the accumulation of the neuronal internal variable can be viewed as an integration. When the intensity λ integrates to one, the neuron fires deterministically:

$$\int_0^{t_{\text{fire}}} \lambda(t) dt = \int_0^{t_{\text{fire}}} h e^{ax(t)} dt = 1. \quad (\text{D5})$$

Further, we assume that when the spiking is very frequent, the relaxation does not play significant roles. Then we have $x(t) = \beta \cdot \mu t$, where $\beta \cdot \mu = \sum_{\text{input } j} \beta_j \mu_j$. Together with Eq. (D5), we can solve t_{fire} :

$$t_{\text{fire}} = \frac{1}{a\beta \cdot \mu} \ln \left(1 + \frac{a\beta \cdot \mu}{h} \right). \quad (\text{D6})$$

The n -th moment of the intensity λ is given by

$$\mathbb{E}[\lambda^n] = \frac{1}{t_{\text{fire}}} \int_0^{t_{\text{fire}}} h^n e^{nax(t)} dt = \frac{h^n (e^{na\beta \cdot \mu t_{\text{fire}}} - 1)}{na\beta \cdot \mu t_{\text{fire}}}. \quad (\text{D7})$$

Specifically, the mean and variance of λ are

$$\mathbb{E}[\lambda] = \frac{1}{t_{\text{fire}}}, \quad \mathbb{V}[\lambda] = \frac{h^2 (e^{2a\beta \cdot \mu t_{\text{fire}}} - 1)}{2a\beta \cdot \mu t_{\text{fire}}} - \frac{1}{t_{\text{fire}}^2}. \quad (\text{D8})$$

The k -th moment of x can be calculated:

$$\mathbb{E}[x^k] = \frac{1}{t_{\text{fire}}} \int_0^{t_{\text{fire}}} (\beta \cdot \mu)^k t^k dt = \frac{(\beta \cdot \mu)^k}{k+1} t_{\text{fire}}^k. \quad (\text{D9})$$

Specifically, the mean and variance of x are

$$\mathbb{E}[x] = \frac{\beta \cdot \mu}{2} t_{\text{fire}}, \quad \mathbb{V}[x] = \frac{(\beta \cdot \mu)^2}{12} t_{\text{fire}}^2. \quad (\text{D10})$$

3. TMF limits with relaxation

Similarly to the previous case, but when the spiking is not frequent and relaxation cannot be neglected, we have $x(t) = \beta \cdot \mu \tau (1 - e^{-t/\tau})$. Integrate Eq. (D5) and we can solve t_{fire} from the following equation

$$h\tau e^{a\beta \cdot \mu \tau} \left[\text{Ei}(-a\beta \cdot \mu \tau) - \text{Ei}(-a\beta \cdot \mu \tau e^{-t_{\text{fire}}/\tau}) \right] = 1. \quad (\text{D11})$$

This can be done similarly as solving Eq. (B2) in Appendix B.

The n -th moment of intensity λ is given by

$$\begin{aligned} \mathbb{E}[\lambda^n] \\ = \frac{h^n \tau e^{na\beta \cdot \mu \tau}}{t_{\text{fire}}} \left[\text{Ei}(-na\beta \cdot \mu \tau) - \text{Ei}(-na\beta \cdot \mu \tau e^{-\frac{t_{\text{fire}}}{\tau}}) \right]. \end{aligned} \quad (\text{D12})$$

Specifically, the mean and variance of λ are

$$\mathbb{E}[\lambda] = \frac{1}{t_{\text{fire}}}, \quad \mathbb{V}[\lambda] = \mathbb{E}[\lambda^2] - \frac{1}{t_{\text{fire}}^2}. \quad (\text{D13})$$

The k -th moment ($k \geq 1$) of x can be calculated:

$$\mathbb{E}[x^k] = \frac{(\beta \cdot \mu)^k}{t_{\text{fire}}} \int_0^{t_{\text{fire}}} (1 - e^{-t/\tau})^k dt. \quad (\text{D14})$$

Specifically, the mean of x is

$$\mathbb{E}[x] = \frac{\beta \cdot \mu \tau}{t_{\text{fire}}} \left[t_{\text{fire}} + \tau (e^{-t_{\text{fire}}/\tau} - 1) \right] \quad (\text{D15})$$

and the variance of x is

$$\begin{aligned} \mathbb{V}[x] \\ = \frac{(\beta \cdot \mu)^2 \tau^3 \left(1 - e^{-\frac{t_{\text{fire}}}{\tau}} \right) \left(e^{-\frac{t_{\text{fire}}}{\tau}} (t_{\text{fire}} + 2\tau) + t_{\text{fire}} - 2\tau \right)}{2t_{\text{fire}}^2} \end{aligned} \quad (\text{D16})$$

[1] A. Arieli, A. Sterkin, A. Grinvald, and A. Aertsen, Dynamics of ongoing activity: Explanation of the large variability in evoked cortical responses, *Science* **273**, 1868 (1996).

[2] Z. Mainen and T. Sejnowski, Reliability of spike timing in neocortical neurons, *Science* **268**, 1503 (1995).

[3] W. H. Calvin and C. F. Stevens, Synaptic noise as a source of variability in the interval between action potentials, *Science* **155**, 842 (1967).

[4] W. Bialek, Physical limits to sensation and perception, *Annual review of biophysics and biophysical chemistry* **16**, 455 (1987).

[5] M. L. Schölvicck, A. Maier, Q. Y. Frank, J. H. Duyn, and D. A. Leopold, Neural basis of global resting-state fmri activity, *Proceedings of the National Academy of Sciences* **107**, 10238 (2010).

[6] F. Briggs, G. R. Mangun, and W. M. Usrey, Attention enhances synaptic efficacy and the signal-to-noise ratio in neural circuits, *Nature* **499**, 476 (2013).

[7] R. B. Stein, E. R. Gossen, and K. E. Jones, Neuronal variability: noise or part of the signal?, *Nature Reviews Neuroscience* **6**, 389 (2005).

[8] A. A. Faisal, L. P. Selen, and D. M. Wolpert, Noise in the nervous system, *Nature reviews neuroscience* **9**, 292 (2008).

[9] L. Q. Uddin, Bring the noise: Reconceptualizing spontaneous neural activity, *Trends in Cognitive Sciences* (2020).

[10] M. Abeles, H. Bergman, I. Gat, I. Meilijson, E. Seidenmann, N. Tishby, and E. Vaadia, Cortical activity flips among quasi-stationary states, *Proceedings of the National Academy of Sciences* **92**, 8616 (1995).

[11] E. Tognoli and J. S. Kelso, The metastable brain, *Neuron* **81**, 35 (2014).

[12] S. Karlin, *A first course in stochastic processes* (Academic press, 2014).

[13] E. Parzen, *Stochastic processes* (SIAM, 1999).

[14] D. J. Daley and D. Vere-Jones, An introduction to the theory of point processes. vol. i. probability and its applications (2003).

[15] D. J. Daley and D. Vere-Jones, *An introduction to the theory of point processes: volume II: general theory and structure* (Springer Science & Business Media, 2007).

[16] D. Labarre, W. Meissner, and T. Boraud, Measure of the regularity of events in stochastic point processes, application to neuron activity analysis, in *2008 IEEE International Conference on Acoustics, Speech and Signal Processing* (IEEE, 2008) pp. 489–492.

[17] W. Truccolo, U. T. Eden, M. R. Fellows, J. P. Donoghue, and E. N. Brown, A point process framework for relating neural spiking activity to spiking history, neural ensemble, and extrinsic covariate effects, *Journal of neurophysiology* **93**, 1074 (2005).

[18] F. Gerhard, M. Deger, and W. Truccolo, On the stability and dynamics of stochastic spiking neuron models: Nonlinear hawkes process and point process glms, *PLoS computational biology* **13**, e1005390 (2017).

[19] A. N. Burkitt, A review of the integrate-and-fire neuron model: I. homogeneous synaptic input, *Biological cybernetics* **95**, 1 (2006).

[20] S.-I. Amari, Homogeneous nets of neuron-like elements, *Biological cybernetics* **17**, 211 (1975).

[21] O. D. Faugeras, J. D. Touboul, and B. Cessac, A constructive mean-field analysis of multi population neural networks with random synaptic weights and stochastic inputs, *Frontiers in computational neuroscience* **3**, 1 (2009).

[22] J. Touboul, G. Hermann, and O. Faugeras, Noise-induced behaviors in neural mean field dynamics, *SIAM Journal on Applied Dynamical Systems* **11**, 49 (2012).

[23] L. Cossell, M. F. Iacaruso, D. R. Muir, R. Houlton, E. N. Sader, H. Ko, S. B. Hofer, and T. D. Mrsic-Flogel, Functional organization of excitatory synaptic strength in primary visual cortex, *Nature* **518**, 399 (2015).

[24] W.-C. A. Lee, V. Bonin, M. Reed, B. J. Graham, G. Hood, K. Glattfelder, and R. C. Reid, Anatomy and function of an excitatory network in the visual cortex, *Nature* **532**, 370 (2016).

[25] F. Baccelli and T. Taillefumier, Replica-mean-field limits for intensity-based neural networks, *SIAM Journal on Applied Dynamical Systems* **18**, 1756 (2019).

[26] M. Mézard and G. Parisi, Replicas and optimization, *Journal de Physique Lettres* **46**, 771 (1985).

[27] M. Mézard and G. Parisi, Statistical physics of structural glasses, *Journal of Physics: Condensed Matter* **12**, 6655 (2000).

[28] M. Benaim and J.-Y. Le Boudec, A class of mean field interaction models for computer and communication systems, *Performance evaluation* **65**, 823 (2008).

[29] C.-S. Choi and F. Baccelli, An analytical framework for coverage in cellular networks leveraging vehicles, *IEEE Transactions on Communications* **66**, 4950 (2018).

[30] F. Baccelli, M. Davydov, and T. Taillefumier, Replica-mean-field limits of fragmentation-interaction-aggregation processes, *arXiv preprint arXiv:2005.07962* (2020).

[31] K. Matthes, Zur Theorie der Bedienungsprozesse, in *Trans. Third Prague Conf. Information Theory, Statist. Decision Functions, Random Processes (Liblice, 1962)* (Publ. House Czech. Acad. Sci., Prague, 1964) pp. 513–528.

[32] T. Taillefumier, J. Touboul, and M. Magnasco, Exact event-driven implementation for recurrent networks of stochastic perfect integrate-and-fire neurons, *Neural Computation* **24**, 3145 (2012).

[33] R. Moreno-Bote, J. Rinzel, and N. Rubin, Noise-induced alternations in an attractor network model of perceptual bistability, *Journal of neurophysiology* **98**, 1125 (2007).

[34] Y. Kuang, *Delay differential equations* (University of California Press, 2012).

[35] L. Torelli, Stability of numerical methods for delay differential equations, *Journal of Computational and Applied Mathematics* **25**, 15 (1989).

[36] R. D. Driver, *Ordinary and delay differential equations*, Vol. 20 (Springer Science & Business Media, 2012).

[37] F. M. Asl and A. G. Ulsoy, Analysis of a system of linear delay differential equations, *J. Dyn. Sys., Meas., Control* **125**, 215 (2003).

[38] S. Teitler and R. Wallis, Liouville equation and the resolvent formalism, *Journal of Mathematical Physics* **1**, 372 (1960).

[39] I. M. Gel'fand and L. Dikii, Asymptotic behaviour of the

resolvent of sturm-liouville equations and the algebra of the korteweg-de vries equations, *Russian Mathematical Surveys* **30**, 77 (1975).

[40] M. Schönberg, Physical applications of the resolvent operators on the mathematical formalism of feynman's theory of the positron, *Il Nuovo Cimento (1943-1954)* **8**, 651 (1951).

[41] A. De Masi, A. Galves, E. Löcherbach, and E. Presutti, Hydrodynamic limit for interacting neurons, *Journal of Statistical Physics* **158**, 866 (2015).

[42] H. E. Plesser and S. Tanaka, Stochastic resonance in a model neuron with reset, *Physics Letters A* **225**, 228 (1997).

[43] S. P. Meyn and R. L. Tweedie, Stability of markovian processes iii: Foster-lyapunov criteria for continuous-time processes, *Advances in Applied Probability* **25**, 518 (1993).

[44] F. Baccelli and T. Taillefumier, The pair-replica-mean-field limit for intensity-based neural networks, *SIAM Journal on Applied Dynamical Systems* **20**, 165 (2021).

[45] A. N. Rybko and S. B. Shlosman, Poisson hypothesis for information networks. i, *Moscow mathematical journal* **5**, 679 (2005).

[46] M. Miyazawa, The intensity conservation law for queues with randomly changed service rate, *Journal of applied probability* , 408 (1985).

[47] F. Baccelli and P. Brémaud, The palm calculus of point processes, in *Elements of Queueing Theory* (Springer, 2003) pp. 1–74.

[48] T. Kato, *Perturbation theory for linear operators*, Vol. 132 (Springer Science & Business Media, 2013).

[49] V. Daftardar-Gejji and H. Jafari, An iterative method for solving nonlinear functional equations, *Journal of Mathematical Analysis and Applications* **316**, 753 (2006).

[50] E. Weinan, *Principles of multiscale modeling* (Cambridge University Press, 2011).

[51] C. M. Bender and S. A. Orszag, *Advanced mathematical methods for scientists and engineers I: Asymptotic methods and perturbation theory* (Springer Science & Business Media, 2013).

[52] W. Van Assche, Padé and hermite-padé approximation and orthogonality, *arXiv preprint math/0609094* (2006).

[53] C. M. Bender and S. A. Orszag, *Advanced mathematical methods for scientists and engineers I: Asymptotic methods and perturbation theory* (Springer Science & Business Media, 2013).

[54] C. Van Vreeswijk and H. Sompolinsky, Chaos in neuronal networks with balanced excitatory and inhibitory activity, *Science* **274**, 1724 (1996).

[55] P. C. Bressloff, Metastable states and quasicycles in a stochastic wilson-cowan model of neuronal population dynamics, *Phys. Rev. E* **82**, 051903 (2010).

[56] M. I. Rabinovich, R. Huerta, P. Varona, and V. S. Afraimovich, Transient cognitive dynamics, metastability, and decision making, *PLoS Comput Biol* **4**, e1000072 (2008).

[57] J. S. Kelso and E. Tognoli, Metastability in the brain, in *The 2006 IEEE International Joint Conference on Neural Network Proceedings* (IEEE, 2006) pp. 363–368.

[58] G. Werner, Metastability, criticality and phase transitions in brain and its models, *Biosystems* **90**, 496 (2007).

[59] P. Bressloff and J. Newby, Metastability in a stochastic neural network modeled as a velocity jump markov process, *SIAM Journal on Applied Dynamical Systems*, *SIAM Journal on Applied Dynamical Systems* **12**, 1394 (2013).

[60] C. Kemere, G. Santhanam, B. M. Yu, A. Afshar, S. I. Ryu, T. H. Meng, and K. V. Shenoy, Detecting neural-state transitions using hidden markov models for motor cortical prostheses, *Journal of neurophysiology* **100**, 2441 (2008).

[61] L. Rabiner and B. Juang, An introduction to hidden markov models, *ieee assp magazine* **3**, 4 (1986).

[62] D. J. Aldous, Exchangeability and related topics, in *École d'Été de Probabilités de Saint-Flour XIII—1983* (Springer, 1985) pp. 1–198.

[63] G. Buzsáki and K. Mizuseki, The log-dynamic brain: how skewed distributions affect network operations, *Nature Reviews Neuroscience* **15**, 264 (2014).

[64] W. Gerstner, W. M. Kistler, R. Naud, and L. Paninski, *Neuronal dynamics: From single neurons to networks and models of cognition* (Cambridge University Press, 2014).

[65] P. Brémaud and L. Massoulié, Stability of nonlinear hawkes processes, *The Annals of Probability* , 1563 (1996).

[66] E. V. Lubenov and A. G. Siapas, Decoupling through synchrony in neuronal circuits with propagation delays, *Neuron* **58**, 118 (2008).

[67] J. Eggermont, Peripheral auditory adaptation and fatigue: a model oriented review, *Hearing research* **18**, 57 (1985).

[68] M. M. Rolls, D. Satoh, P. J. Clyne, A. L. Henner, T. Uemura, and C. Q. Doe, Polarity and intracellular compartmentalization of drosophila neurons, *Neural development* **2**, 1 (2007).

[69] F. C. Hoppensteadt, *An introduction to the mathematics of neurons: modeling in the frequency domain* (Cambridge University Press, 1997).

[70] G. A. Baker Jr, A theorem on the convergence of padé approximants, *Studies in Applied Mathematics* **55**, 107 (1976).

[71] L. Arnold, Random dynamical systems, in *Dynamical systems* (Springer, 1995) pp. 1–43.

[72] C. W. Gardiner *et al.*, *Handbook of stochastic methods*, Vol. 3 (springer Berlin, 1985).

[73] S. S. Varadhan, *Large deviations and applications* (SIAM, 1984).